SANDIA REPORT

SAND2005-6758
Unlimited Release
Printed October 2005

Shock-Induced Explosive Chemistry in a Deterministic Sample Configuration

Wayne M. Trott, Melvin R. Baer, Jaime N. Castañeda, Alexander S. Tappan, John N. Stuecker, and Joseph Cesarano III

Prepared by
Sandia National Laboratories
Albuquerque, New Mexico 87185 and Livermore, California 94550

Sandia is a multiprogram laboratory operated by Sandia Corporation, a Lockheed Martin Company, for the United States Department of Energy's National Nuclear Security Administration under Contract DE-AC04-94AL85000.

Issued by Sandia National Laboratories, operated for the United States Department of Energy by Sandia Corporation.

Available to DOE and DOE contractors from
U.S. Department of Energy
Office of Scientific and Technical Information
P.O. Box 62
Oak Ridge, TN 37831

Telephone: (865)576-8401
Facsimile: (865)576-5728
E-Mail: reports@adonis.osti.gov
Online ordering: http://www.osti.gov/bridge

Available to the public from
U.S. Department of Commerce
National Technical Information Service
5285 Port Royal Rd
Springfield, VA 22161

Telephone: (800)553-6847
Facsimile: (703)605-6900
E-Mail: orders@ntis.fedworld.gov
Online order: http://www.ntis.gov/help/ordermethods.asp?loc=7-4-0#online

SAND2005-6758
Unlimited Release
Printed October 2005

Shock-Induced Explosive Chemistry in a Deterministic Sample Configuration

Wayne M. Trott, Melvin R. Baer, Jaime N. Castañeda
Engineering Sciences Center

Alexander S. Tappan
Explosive Projects and Diagnostics Department

John N. Stuecker and Joseph Cesarano III
Ceramic Processing and Inorganic Materials Department

Sandia National Laboratories
P.O. Box 5800
Albuquerque, New Mexico 87185-0834

Abstract

Explosive initiation and energy release have been studied in two sample geometries designed to minimize stochastic behavior in shock-loading experiments. These sample concepts include a design with explosive material occupying the hole locations of a close-packed bed of inert spheres and a design that utilizes infiltration of a liquid explosive into a well-defined inert matrix. Wave profiles transmitted by these samples in gas-gun impact experiments have been characterized by both velocity interferometry diagnostics and three-dimensional numerical simulations. Highly organized wave structures associated with the characteristic length scales of the deterministic samples have been observed. Initiation and reaction growth in an inert matrix filled with sensitized nitromethane (a homogeneous explosive material) result in wave profiles similar to those observed with heterogeneous explosives. Comparison of experimental and numerical results indicates that energetic material studies in deterministic sample geometries can provide an important new tool for validation of models of energy release in numerical simulations of explosive initiation and performance.

Acknowledgments

This project, LDRD 05-0483, “Shock-Induced Explosive Chemistry in a Deterministic Sample Configuration,” was a one-year exploratory effort funded by the Laboratory Directed Research and Development (LDRD) program at Sandia National Laboratories. The authors thank Lloyd Bonzon and operations personnel at the Sandia Explosive Components Facility gas gun for their help and cooperation in the execution of the experiments described here. In particular, the excellent technical assistance of John Liwski and Heidi Anderson is gratefully acknowledged.

Table of Contents

List of Figures

List of Figures (cont.)

List of Tables

1. Introduction

Despite decades of active research, the current understanding of reactive flow in solid explosives is still surprisingly rudimentary, depending on (1) experiments that typically access average behavior (only) in highly specific sample configurations and (2) models that are purely phenomenological. In heterogeneous energetic materials, the shock sensitivity of initiation and sustained reaction is intimately tied to processes occurring at the grain or crystal level. Shock wave fields are three-dimensional and unsteady arising first at contact points and then coalescing to produce a complex distribution of thermal and mechanical states that are, in turn, highly coupled to fundamental chemical processes of the energetic material.[1] These processes are driven by the highly localized temperature and stress states of the material; the size, intensity and distribution as well as the coalescence of resulting "hot spots" within the shock-loaded material are considered to be controlling factors in initiation and growth of reaction. Unfortunately, in typical heterogeneous explosive formulations (pressed, granular explosive with or without added binder materials), "hot spot" formation and growth is highly stochastic in nature. The complex statistics is a significant barrier to identification and analysis of the important underlying chemistry.

In this report, we explore different approaches to preparing and testing explosive samples in a highly deterministic configuration. The intent is to preserve the essential phenomenology of heterogeneous explosive initiation (a wide range of stress and temperature with extreme conditions localized at contact points and interfaces) while largely constraining stochastic behavior. We have examined two concepts in detail: (1) a target design with explosive material occupying the hole locations of a close-packed bed of inert spheres and (2) infiltration of a liquid explosive into a well-defined rod array formed by Sandia's Robocasting process. We have evaluated the mesoscale shock response of deterministic samples of this type (in well controlled gas-gun impact studies) by performing transmitted wave profile measurements using both single-point velocity interferometry system for any reflector (VISAR) and the high-spatial-resolution capabilities of a line-imaging optically recording velocity interferometer system (ORVIS). Experimental data are compared to results of three-dimensional numerical simulations in order to evaluate this combined experimental and numerical methodology as a path forward to the crucial development of a predictive capability for explosive chemistry in more general applications containing a large degree of stochastic behavior.

The remainder of this report is organized in the following manner. Section 2 provides a necessary review of previous work leading up to this investigation of deterministic sample geometries and also gives a brief overview of the available experimental and numerical tools. Section 3 summarizes our preliminary results with the sample concept involving highly organized lattices of sub-millimeter-scale inert and/or explosive spheres. Section 4 provides a detailed look at the deterministic sample geometry involving Robocast inserts. This section contains a description of the Robocast insert fabrication process as well as procedures for target assembly and liquid explosive sample loading. Comparison and analysis of experimental wave profile data and 3-D numerical simulations comprise the principal discussion in this section. Finally, a summary and recommendations for future work in this research area are contained in Section 5.

2. Review of Previous Work and Experimental/Numerical Methods

2.1 Motivation

Analysis of detailed shock response in heterogeneous materials is addressed by current capabilities for three-dimensional (3-D) numerical simulations.[1] These calculations explore the correlation between microscopic properties and the response of the material at mesoscopic scales, including detailed spatial and temporal variations in stress and thermal fields (dispersive behavior). To support the computational efforts, line-imaging velocity interferometry methods have been developed and utilized to investigate shock behavior at mesoscopic scales in a variety of materials subjected to impact loading in gas-gun tests.[2] Although details of wave behavior within the heterogeneous material cannot be directly probed using these methods, important interactions at physical boundaries can be observed. The integration of mesoscale modeling with time-resolved and spatially resolved experimental measurement techniques offers much promise to improve our understanding of the shock response of heterogeneous materials by providing useful information for validation and calibration of the models.

Our initial efforts to explore shock propagation in a deterministic sample geometry were motivated by gas-gun studies of waves transmitted by low-density (65% TMD (theoretical maximum density)) pressings of HMX (1,3,5,7-tetranitro-1,3,5,7-tetraazacyclooctane).[3] Wave profiles generated by sieved, coarse-grain (212 – 300 μm) HMX are particularly interesting in that they exhibit distinct ordered wave structures that appear to be both distributed over multiple grain dimensions and largely coherent temporally. It is likely that these features are driven in part by the tendency of nearly monodisperse particles to pack in a somewhat layered structure. For a reactive material, the higher shock-induced temperatures ("hot spots" and high-temperature regions localized near grain boundaries) that would be generated primarily in the layered void volume are likely to produce ignition in a pattern that is somewhat correlated with this packing geometry. This pattern may, in turn, imprint a near-periodic signature on the emerging wave front. Detailed analysis of this scenario via 3-D numerical mesoscale computation would require an adequate description of the actual mesostructure that still involves some stochastic elements. One important factor is the extent and morphology of crystal fracture which occurs to a significant degree even in pressings to only 65% TMD. These physical factors exacerbate the uncertainty that currently exists on the mechanisms and reaction rates needed to model the reactive waves accurately. An important step in the development of this analysis is the quantitative evaluation (both experimental and theoretical) of limiting cases; e.g., a sample with simplified geometry and material properties. Accordingly, we developed methods for investigating the response of a porous lattice of close-packed metal spheres.[4] This approach provides a favorable opportunity to relate measured wave structures to a well-characterized sample microstructure.

2.2 Initial Tests and Experimental Methods

In our initial attempt at developing a deterministic sample geometry, we adapted the gas gun target design used in the earlier HMX experiments to probe close-packed samples of tin spheres. A schematic diagram of this design is shown in Fig. 1. The

experimental assembly consists of a Kel-F impactor and a Kel-F sample cup containing the bed of spherical particles. A 0.225-mm-thick buffer layer of Kapton (not shown) and an aluminized PMMA (poly(methyl methacrylate)) interferometer window confine the porous bed. The target fixture is designed to accommodate simultaneous measurements using a fiber-coupled, single-point VISAR and a line-imaging optically recording velocity interferometer system (ORVIS). The Kapton buffer is used to mitigate the loss in reflected light intensity that can occur upon shock arrival at the window.

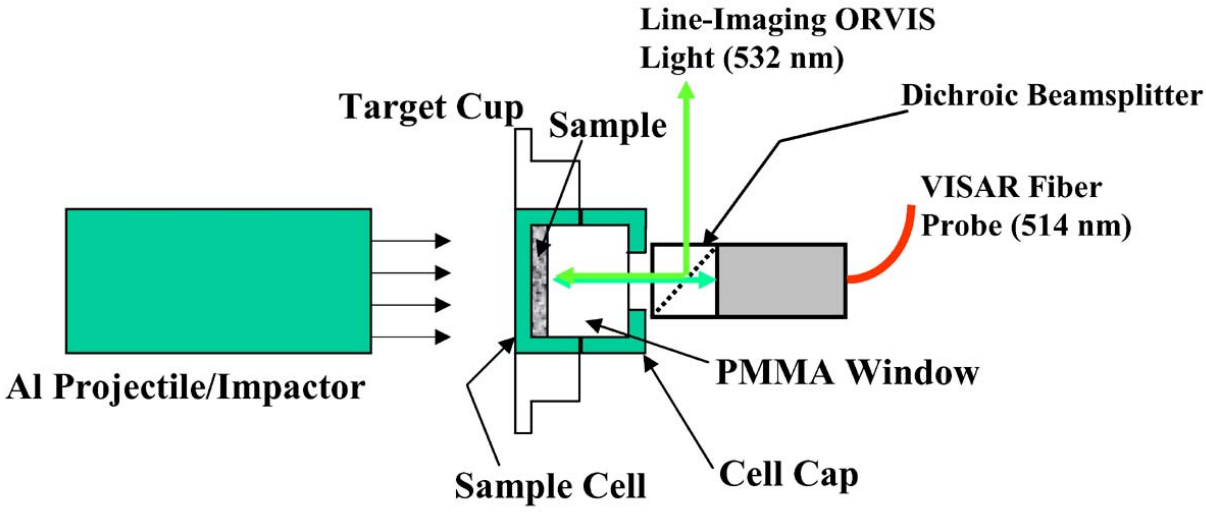

Figure 1. Schematic diagram of gas-gun target with associated diagnostics.

The velocity interferometry diagnostics employed in this study included dual-delay-leg, "push-pull" VISAR instrumentation for single-point measurements and a line-imaging ORVIS for spatially resolved measurements capable of probing mesoscopic scale phenomena. The line-imaging ORVIS is an adaptation of the single-spot ORVIS instrumentation developed approximately two decades ago by Bloomquist and Sheffield.[5] The feasibility of operation of an ORVIS in a line-imaging mode was demonstrated and reported in 1995 by Baumung et al.[6] We have retained many important aspects of the approach of Baumung et al. while implementing a number of useful changes in the laser illumination and light collection optics as well as in data reduction and analysis methods.[2,7,8] This effort has been directed toward the development of an optimized probe for elucidating the mesoscale shock response of granular materials.

The essential aspects of the line-imaging ORVIS design are illustrated schematically in Fig. 2. As in the conventional ORVIS configuration, coherent light from the source laser is focused onto the target of interest (cf. Fig. 1). Efficient illumination of the target along a line segment is provided by a combination of spherical and cylindrical lenses similar to that used in well-established methods for laser light sheet generation.[9] This approach enables independent tailoring of the width and length of the line segment on target. The lens combination includes one spherical component and an associated cylindrical lens that are positioned to transform the collimated laser beam into a line of minimal width (~100 μm). This is accomplished by locating the cylindrical lens at twice its focal length from the target and the spherical lens at an additional distance equal to its focal length plus the target/cylindrical lens distance. By separating the optics in this

manner, the cylindrical lens is used to image the small diameter of the focal spot of the first lens to the target in one dimension. The length of the line segment, on the other hand, is determined by the positions and focal lengths of two additional cylindrical lenses (both oriented 90^{o} to the cylindrical lens described above) in combination with the spherical lens. With the position of the spherical lens fixed to provide the minimal line width, these cylindrical lenses are moved (essentially in tandem) to vary the line length as desired. If the laser source can provide sufficient intensity for the experiment, nearly uniform illumination can be achieved over several mm in the horizontal dimension by using only the center portion of a relatively long line.

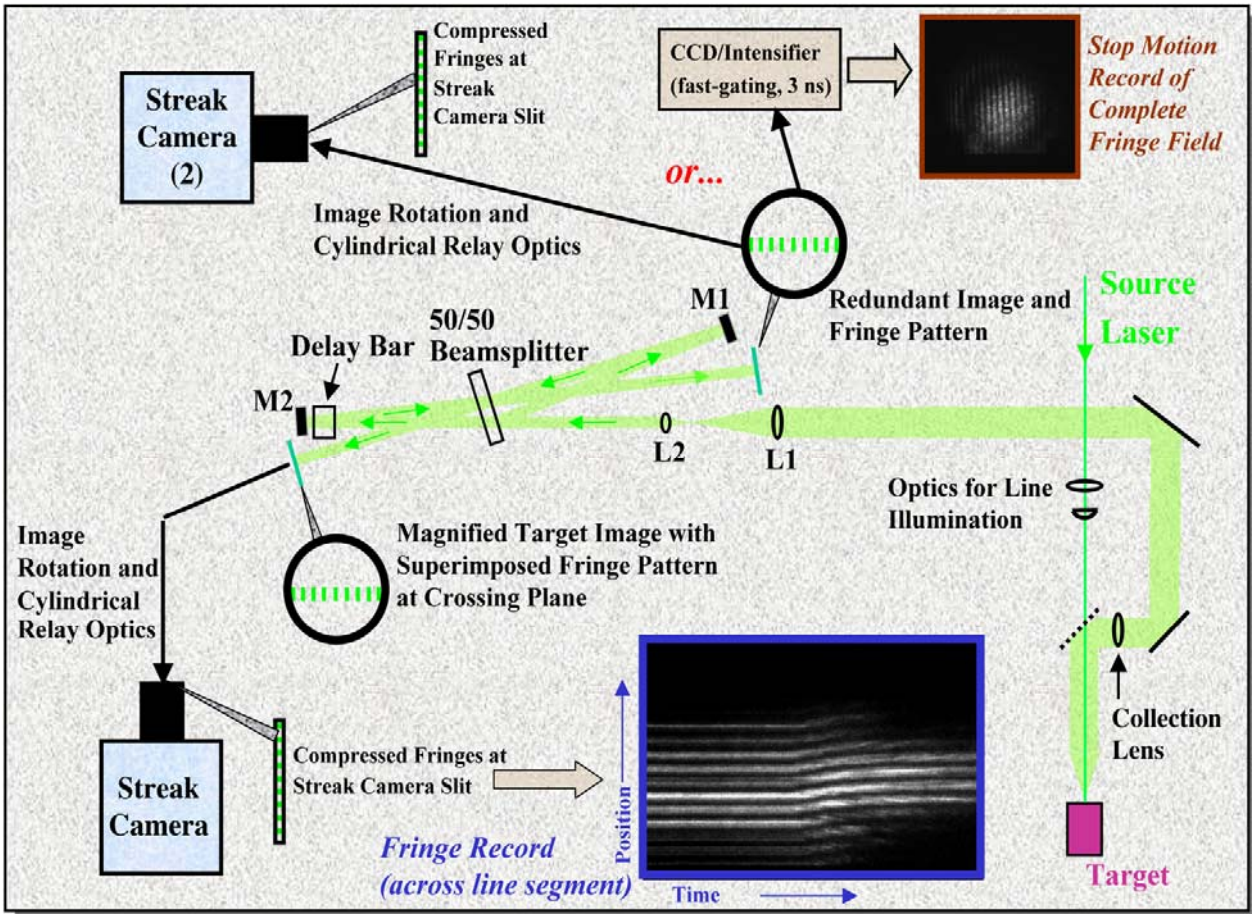

Figure 2. Schematic diagram of a line-imaging optically recording velocity interferometer system (ORVIS).

Before reaching the target, the input light passes though a custom-manufactured, polarization-sensitive beamsplitter (CVI Laser, Inc.). This optical component is designed to transmit horizontally polarized laser light (Nd:YVO_4 laser, 532 nm) at an efficiency of 80 percent and to reflect the largely unpolarized light from the target at an efficiency of 42 percent, providing a significantly higher overall efficiency than a simple 50/50 beamsplitter. Better light transmission can often be achieved with a turning mirror equipped with a small central hole; however, we found it very advantageous to avoid

issues of on-axis image degradation typically encountered with this arrangement. The collection lens shown in Fig. 2 both collects and roughly collimates the diffusely reflected light from the target. The collimated beam is then directed to the interferometer assembly by a series of turning mirrors. Before entering the interferometer, the beam is reduced in diameter by the down-collimating telescope optics (L1 and L2, respectively, in Fig. 2).

A 50/50 beamsplitter divides the beam into two equal-intensity components, one of which serves as a reference leg. The second leg passes through a variable-length fused silica cylinder. This optical component imparts a time delay (proportional to the cylinder length) in the second beam. Observed motion of the interference fringes generated by beam recombination (with mirrors tilted so as to produce a "straight-line" pattern) is directly proportional to target velocity. This motion can be recorded by a high-speed streak camera (image rotation and relay optics may be utilized in this operation, depending on the desired location of the streak camera and the orientation of its entrance slit). The collection lens and telescope optics (L1, L2) can be adjusted to produce a magnified image of the target at the recombination plane (i.e., the location of best fringe contrast); in this mode, local variations in target surface velocity are reflected in corresponding local translations of the superimposed fringe field. Facile control of both image size and spatial resolution can be achieved via suitable variations in the relative angles and spacing of the interferometer mirrors as well as the spacing and focal lengths of the imaging optics. Methods for analysis of the streak camera fringe records have been described previously.[7,8]

Operating principles of the VISAR diagnostic have been described in detail elsewhere.[10] Although this system yields data at only a single point, it provides three important advantages. First, simultaneous recording using two legs with different velocity per fringe (VPF) constants promotes unambiguous interpretation of the velocity record. This feature is especially important in data sets involving shock jumps; i.e., interferometer fringe motion that is rapid compared to the system time constant can result in multiple possible solutions in the data analysis for an individual leg. However, only one solution typically satisfies the coupled data sets in a dual-delay-leg setup. As a result, many essential characteristics of the transmitted wave record can be determined with confidence. Second, VISAR data can be recorded on digitizing oscilloscopes with long record lengths, allowing dependable, accurate timing of shock arrival, etc. This feature is very useful in guiding the setup of diagnostics with relatively short recording times; e.g., the high-speed streak camera detection as used in line-imaging ORVIS. Finally, the photomultiplier tube/differential amplifier detection scheme in VISAR is capable of high dynamic range. Hence, signals can be followed and analyzed even under conditions where the reflected light intensity falls off substantially. These advantages proved useful both in the setup of the line-imaging ORVIS and in the subsequent interpretation of the spatially resolved velocity data.

Consistent with the earlier results on sieved HMX, the porous tin-sphere lattices generated transmitted wave profiles with distinct ordered structures. Figure 3 shows a line-imaging ORVIS record of wave behavior obtained with a 5-layer sample (assembled with a hybrid close-packed structure, see Section 2.4 for details) under impact at 0.5 km/s. The spatially resolved velocity profile exhibits an extended precursor region that precedes the main wave by up to 1 μs over some parts of the line segment. This

phenomenon reflects the facile pathways for elastic stress propagation that are available in a highly ordered sample. Also evident are the pronounced ramp wave of ~350ns duration and prominent fluctuations that relate to the particle mesostructure as well as interactions with the interferometer window. Similar temporal variations were seen in the single-point VISAR measurements. These features are in agreement with the results of mesoscale numerical simulations described below.

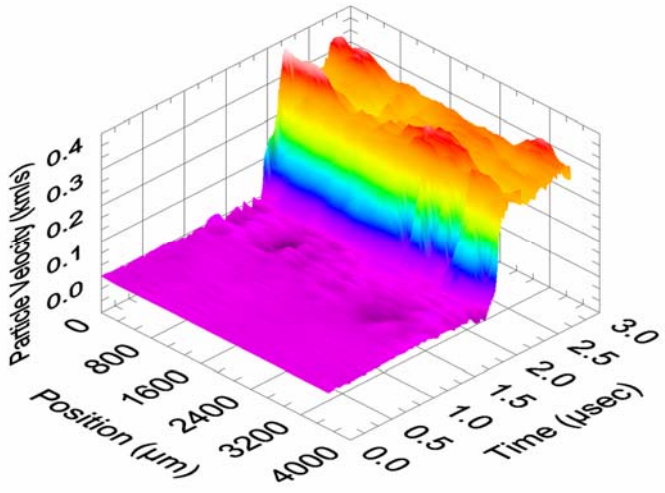

Figure 3. Spatially resolved velocity profile of wave transmitted by close-packed metal spheres.

2.3 Initial Numerical Simulations: Description and Results of Computational Model

Three-dimensional numerical simulations of impact on a lattice of tin spheres were conducted using the Eulerian CTH shock physics code[11] including the projectile and buffer/window materials. In the example shown in Fig. 4, a porous lattice is constructed with five layers of 500-μm diameter tin spheres packed in a close-packed configuration within a representative volume element (RVE) having a transverse and lateral width of 2000 μm × 1800 μm, respectively. This volume of material is sufficient to capture interparticle interactions that are representative of the response of the mesostructure. Periodic boundary conditions are imposed on the transverse boundaries of the RVE. The numerical resolution is fixed at a cell size of 10 μm. Each tin sphere is assigned a distinct material number and material interfaces are allowed to slip in mixed cells. Figure 4 displays the 3-D material geometry prior to impact on the lower surface.

The close packing of spheres forms an initial configuration with a density of ~74% TMD. In this simulation, the tin spheres are assembled in a face centered cubic (*fcc*, also called cubic close packing, *ccp*) orientation in which the geometry of the fourth layer (in the direction of impact) exactly matches that of the first layer and the fifth matches that of the second (often described as ABC-ABC). The alternative close-packed symmetry arrangement, hexagonal close packing (*hcp*), features matching 1-3, 2-4, 3-5, etc. layers (often described as AB-AB). This configuration contains connected voids that propagate, and provide line-of-sight, from the impact face to the probe location. Under impact loading, this condition favors severe, extended material jetting that produces large

perturbations in the wave front, complicating the analysis of particle interactions. Implicit in this direct numerical simulation is the assumption of constitutive relationships that may be only approximate at the mesoscale. Each sphere is modeled using a Mie-Grüneisen EOS and a Steinberg-Guinan-Lund viscoplastic material strength description using CTH EOS database parameters.[12]

A shock load is imparted to the porous lattice by incorporating a symmetric impact of Kel-F onto a Kel-F target layer. Included in the simulations are the Kapton/PMMA materials of the buffer layer and optical window in the gauge package. All of these polymers are modeled using a Maxwell viscoelastic description with the CTH database parameters.[13] Tracers at the Kapton/PMMA interface monitor the conditions at the location of the line-imaging ORVIS.

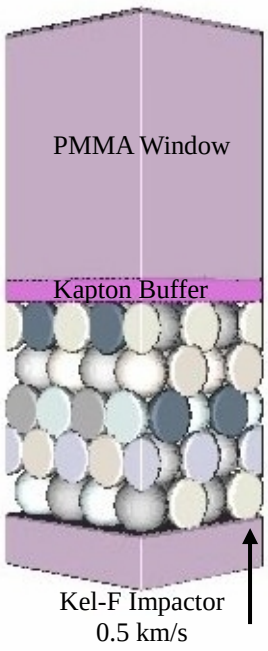

Figure 4. Simulation of tin-sphere shock-loading experiment; initial material configuration prior to impact at 0.5 km/s.

Figure 5 displays a time sequence of material deformation following a 0.5 km/s impact at the lower surface. Painted over the tin surfaces are stress contours. After initial impact, elastic waves traverse the porous layer concentrated at the contact points in the lattice of spheres. Stress bridging is clearly evident as diagonal “fringes” that span the contact points of the tin spheres. As the stress wave propagation continues, material deformation fills the interstitial pores to consolidate the lattice. Material jet effects are evident after 3 μs when the deformed tin spheres interact with the buffer layer interface.

Figure 6 shows a comparison of the spatially-averaged particle velocity measurements to the numerical CTH calculations at the tracer locations on the Kapton/PMMA interface. (The time scale is arbitrarily shifted.) The experimental data and numerical results are very consistent in terms of peak amplitude as well as precursor and ramp durations. As the consolidated lattice interacts with the optical window, wave reflections are produced

by a change in shock impedance. Additional reflections between the consolidated tin layers and the window materials are clearly evident in the computations and are also consistent with the experimental observations. A very important effect seen in the numerical simulations was the markedly different particle velocities generated along orthogonal orientations of the spheres in the lattice packing.[4] This result highlighted the need to develop an improved experimental design featuring precise packing symmetry (instead of the hybrid close packing used to obtain the data in Fig. 3 and Fig. 6, cf. Section 2.4), thereby enabling probe alignment along specified particle orientations.

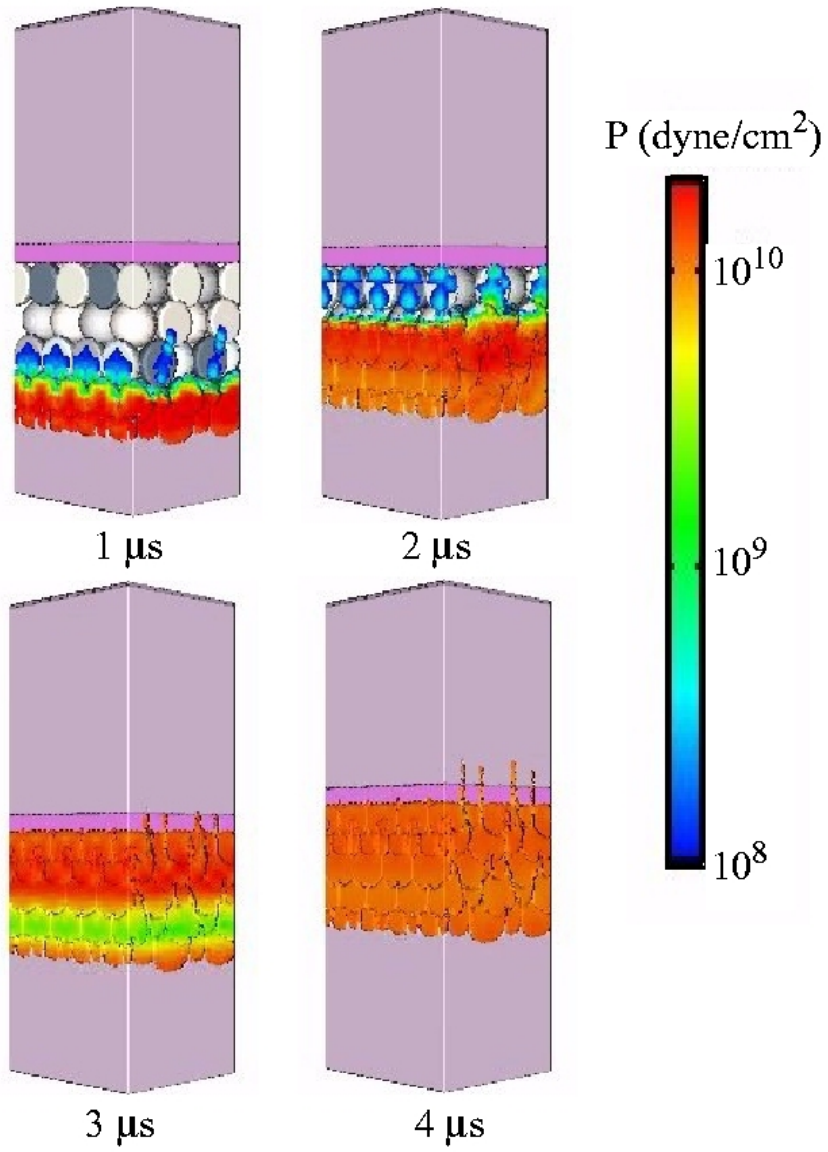

Figure 5. Time sequence of deformation and stress contours in tin-sphere experiment following impact at 0.5 km/s.

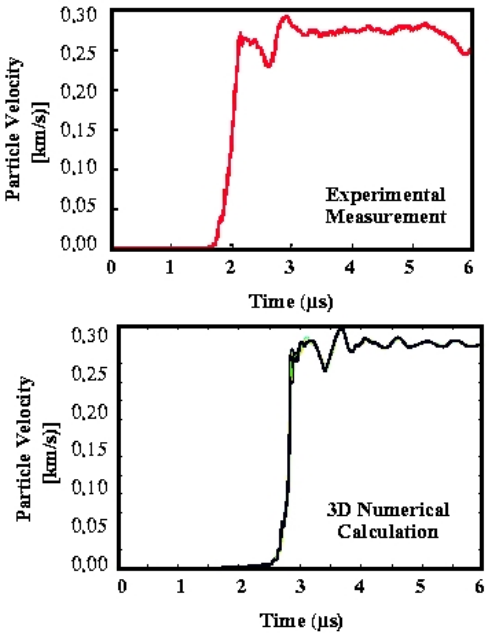

Figure 6. Comparison of experimental and CTH numerical calculations of particle velocity at the buffer/PMMA interface in tin-sphere experiment.

2.4 An Improved Method for Preparing a Precise Face-Centered-Cubic Packing of Metal Spheres

While the Kel-F sample cup (cf. Fig. 1) served as a useful form of confinement for preliminary impact experiments on a close-packed assembly of metal spheres, it is not suited for the precise comparisons that must account for packing symmetry and probe orientation. The deficiencies of the original fixture include the following: (1) the cylindrical sample cup cannot accommodate hexagonal packing in the immediate vicinity of its perimeter—a thin annular region of random packing necessarily occurs in this region; (2) the close-packed spheres are free to orient at various angles about the cylindrical axis of cup, complicating probe orientation in relation to a fixed target mounting position; and (3) as layers are added, there is no engineered method for ensuring a well-defined face-centered cubic (*fcc*) symmetry as utilized in the simulations illustrated in Fig. 5. In order to achieve the desired mesostructure in subsequent experiments, we developed an insert for the sample cup that preserves the appropriate packing symmetry in multiple layers. The design of this fixture is illustrated in the photographs of a prototype aluminum piece shown in Fig. 7.

The prototype piece is intended to accommodate a nine-layer assembly of the 500-μm-diameter spheres. Computational results indicate that the orientation-dependent variations in particle velocity are enhanced as the number of layers increase. The equilateral triangular region proximal to the impact interface (Fig. 7a) is designed for close packing of the spheres, yielding twenty-eight spheres along each side. The photograph showing the first layer in place (Fig. 7b) was taken without illumination from the back. Additional layers are accommodated on an expanding series of carefully machined triangular steps

that result in two additional spheres per side for each step. As Fig. 7c and 7d demonstrate, this arrangement provides for the appropriate *fcc* packing symmetry. Half of the voids shown in Fig. 7b are blocked by the addition of a second layer. In a *hcp* symmetry, the third layer would be positioned directly over the first layer, maintaining connected voids in the positions shown in Fig. 7c. Instead, the fixture design places the third layer in the desired *fcc* orientation, as indicated by full light blockage at the void locations. Succeeding layers maintain this symmetry—the fourth layer replicates the geometry of the first layer, etc., consistent with the packing utilized in the previously described simulations (cf. Fig. 4). A completed nine-layer assembly is shown in Fig. 7e. The triangular shape of the fixture provides a useful reference for precise alignment of the line-imaging ORVIS probe. Hence, this design incorporates important features needed for rigorous comparisons of experiments and mesoscale modeling. Variations on this engineered packing design were considered for application to energetic materials studies, as described in the following section.

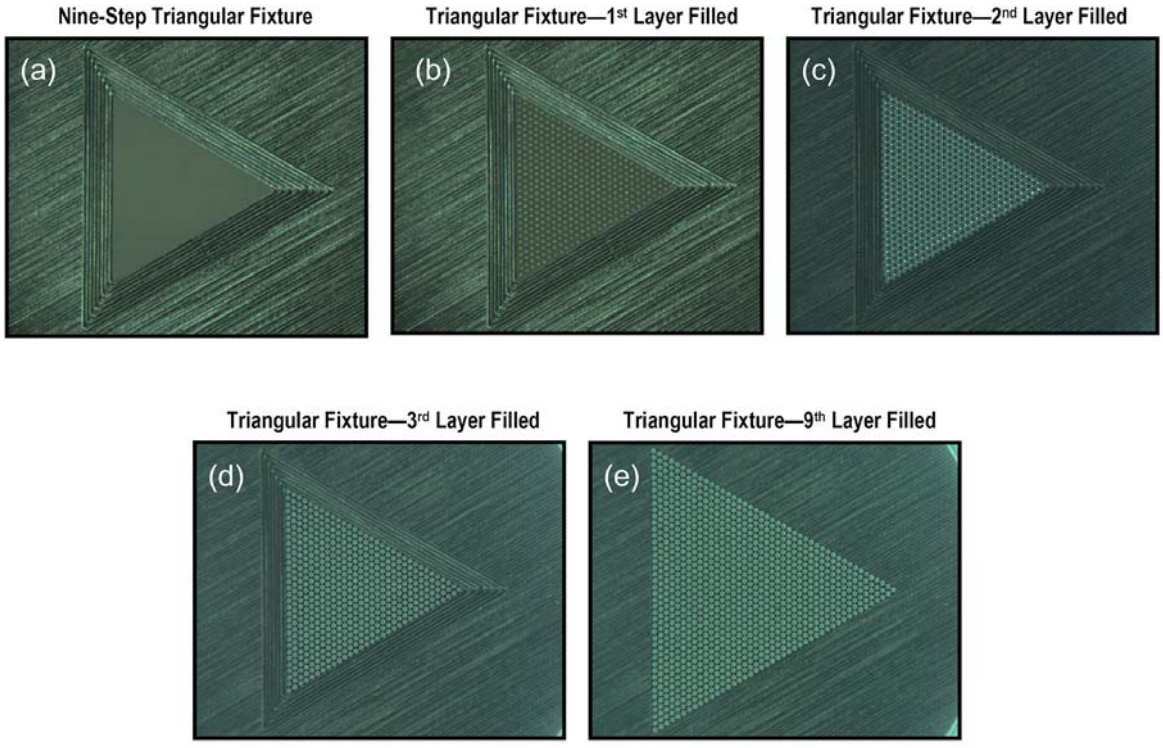

Figure 7. Target sample cup insert for assembly of 500-μm-diameter metal spheres in *fcc* packing arrangement. Photos show the orientation of spheres as layers are filled: (a) fixture before filling; (b) fixture with first layer filled; (c) fixture with second layer filled and light table illumination from below; (d) fixture with third layer filled and light table illumination from below; (e) completed assembly.

3. Initial Concept Evaluation

Realization of an engineered method for preparing close-packed assemblies of metal spheres prompted a follow-on evaluation of a promising concept for organizing energetic materials in a deterministic geometry in order to limit stochastic aspects of initiation and growth processes. This concept involves the positioning of appropriately sized spheres of explosive material in the hole locations of the porous lattice formed by the metal spheres. In a *fcc* packing arrangement of spheres of diameter *d*, for example, voids are regularly distributed and consist of only two sizes: (1) octahedral sites; i.e., regions surrounded by six sample particles and large enough to encompass a sphere of diameter 0.414*d* and (2) tetrahedral sites; i.e., regions surrounded by four sample particles and large enough to accommodate a sphere of diameter 0.225*d*.[14] This design is illustrated by the numerical simulation results shown in Fig. 8. The two sets of graphics show wave propagation in a sample bed consisting of inert tin spheres with nitrocellulose spheres positioned in both types of void location; nitrocellulose is treated as inert in one case and reactive in the other. A pressure-dependent burn model is used to describe the nitrocellulose energy release. This model is likely very simplistic in comparison to the (essentially unknown) details of actual processes of initiation and growth of reaction in the nitrocellulose spheres under such shock-loading conditions but it is instructive as a qualitative description of the phenomenology likely to be observed with this sample geometry. Dramatic wave amplification and induced material jetting are evident in the sample containing the energetic material. Such effects (at an interferometer window interface with the sample) should be accessible to velocity interferometry diagnostics; e.g., the high-speed, spatially resolved material motion sensing capability of the line-imaging ORVIS.

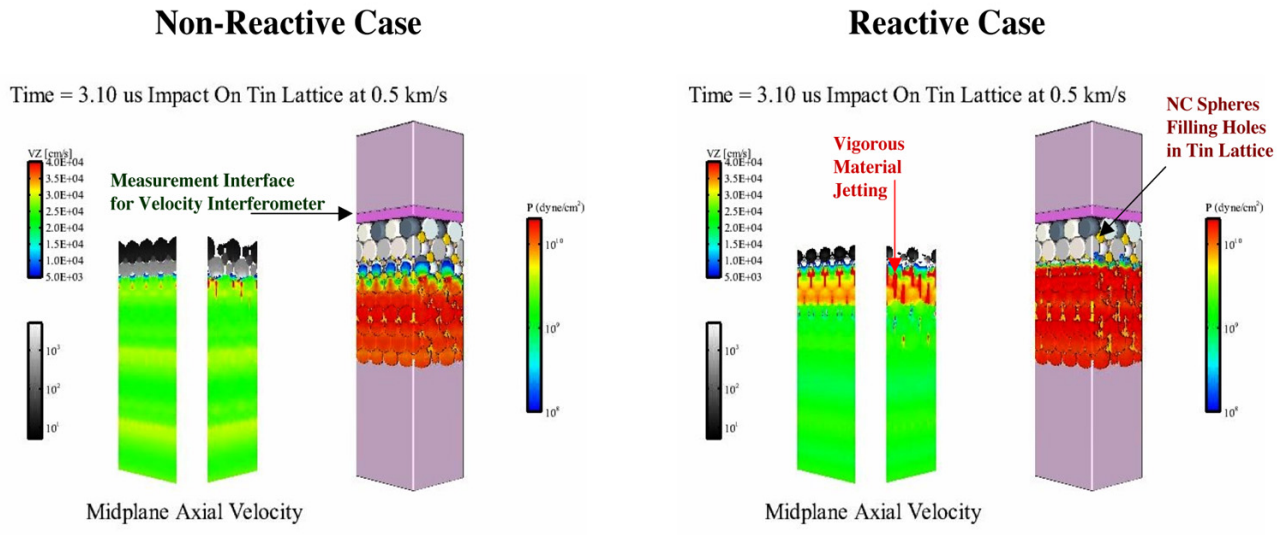

Figure 8. Numerical simulation showing wave propagation with inert (left) and reactive (right) nitrocellulose (NC) spheres positioned in hole locations of a tin sphere lattice.

The target design addressed in Fig. 8 represents a useful approach to satisfy the goal of preserving the essential phenomenology of heterogeneous explosive initiation (a wide range of temperature and stress with critical conditions localized at contact points and interfaces) while largely constraining stochastic behavior. The design also allows several interesting variations (e.g., nitrocellulose spheres replacing the tin spheres or nitrocellulose located in only one class of hole location) that may aid in the interpretation of the relevant chemistry. These variations permit the overall porosity of the sample to be adjusted over a fairly wide range. Comparison of experimental data and numerical simulations pertaining to the highly organized wave structures generated in this type of sample geometry should motivate the development of realistic models of "hot spot" initiation, growth, and coalescence.

We briefly explored methods for assembling the target samples. A hand-assembled mock-up of a low-porosity lattice containing all three sizes of spheres is shown in Fig. 9; 6.35-mm-diameter plastic spheres were used for the primary *fcc* packing. A viable scenario for achieving a low-porosity assembly (and other variations) with spheres of 500-μm-diameter and less would be (1) to utilize a triangular fixture of the type shown in Fig. 7 for assembling each layer of the primary lattice, and (2) to fill in the hole locations with smaller spheres using a programmable two-axis translator coupled to a vacuum pick-up and release device. However, we did not pursue this assembly process further since we were unable to procure energetic materials spheres in the appropriate sizes or in sufficient quantity and purity to build up a reasonable number of gas-gun targets for experimental investigation. Possible suppliers included TNO Prins Maurits Laboratories for spherical RDX and MicroFab Technologies, Inc. for spherical nitrocellulose. Upon inquiry, the RDX material was determined to be both significantly elliptical in shape and too expensive to purchase in quantity. Capabilities for mass production of nitrocellulose spheres are still developing with a current upper limit on diameter of ~80 μm; available spheres are thought to contain appreciable porosity of a variable nature as well.

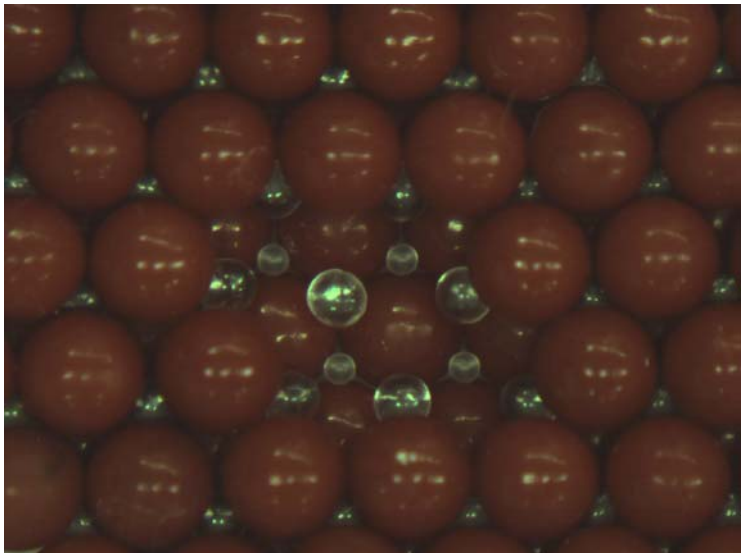

Figure 9. Photograph illustrating a low-porosity packing orientation of sample spheres; the two classes of hole locations generated by the largest spheres are filled by smaller spheres of the appropriate size.

As an alternative to precision assembly of solid spheres of energetic material, we considered the possibility of filling the open volume of a metal-sphere assembly (such as that illustrated in Fig. 7) with a liquid explosive such as nitromethane (NM). The obvious advantage of a liquid sample is that filling of the open volume can be readily achieved in a precise and reproducible manner. We were concerned, however, that NM would not prove sufficiently sensitive to undergo significant reaction growth in the sample geometry of interest (i.e., with the NM distributed in the small-volume hole locations with marginal connectivity between these pockets of energetic material). On the other hand, NM can be sensitized to shock initiation by adding known amounts of a base such as diethylenetriamine (DETA). Before taking the necessary steps to adapt the target fixture described in Section 2.4 to include a liquid fill capability, we decided to perform an initial test using an available set of target hardware originally developed for a project that explored the effects of nano-aluminum on NM initiation and performance.[15] A photograph of the various experimental components including gas-gun target cup, NM sample cup, interferometer window, and fill hardware is shown in Fig. 10.

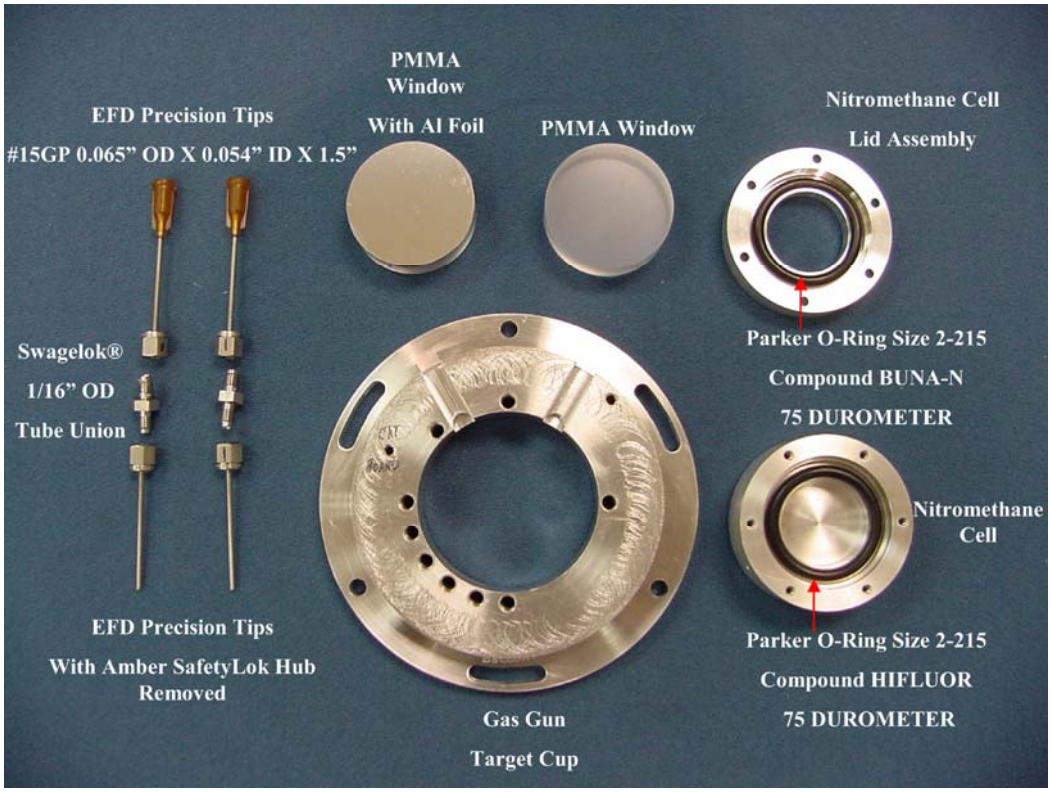

Figure 10. Essential parts for the nitromethane gas gun target assembly described in the text.

The sample volume is defined by a cylindrical cavity (25.4-mm-diameter, 6.4-mm-thick) machined into an aluminum sample cup. For our evaluation test, we filled this volume with 500-μm-diameter tin spheres, carefully adding them layer-by-layer to achieve a fair approximation to a close-packing arrangement. As mentioned above, this form of packing does not ensure a specific *hcp* or *fcc* symmetry and the packing is

necessarily uneven near the perimeter of the cell. On the distal side of this cavity (with respect to the shock propagation direction), the bed of spheres was confined by a 0.225-mm-thick buffer layer of Kapton and an aluminized PMMA disc (12.5-mm-thick) that served as a window for velocity interferometry. As described in Tappan et al.[15], the addition of NM presents significant challenges in terms of material compatibility and in sample loading. It is necessary to design for the following: (1) avoid material degradation and sample leaks, especially under vacuum conditions in the target chamber and (2) allow for rapid sample filling while minimizing the quantity of trapped air. The HIFLUOR O-Ring (cf., Fig. 10) provided a dependable, leak-tight seal between the NM formulations and the Kapton/aluminized PMMA window. Stainless steel fill tubes were used. A nitromethane-compatible adhesive (Barco Bond 5-minute epoxy, Astro Chemical Co.) was used to attach these tubes to the sample cell.

The sample cell was affixed to a target cup that couples the experiment to the barrel of the gas gun. This cup is outfitted with eight time-of-arrival pins that provide projectile velocity and tilt information; one of the velocity pins typically serves as a trigger source for the diagnostics. This test used an aluminum projectile/impactor and was performed at an impact velocity of 1.207 km/s (near the upper limit of velocity for this gas gun).

For preparation of a sensitized NM fill, NM (Aldrich 99+%) and DETA (Aldrich, 99%) were used without further purification. Approximately 3 mL of NM and 10% DETA (by mass) were combined in a 20 mL vial. The vial was stirred with a Teflon-coated stir bar on a magnetic stirring plate for five minutes. Sample preparation was performed immediately before target loading. The NM/DETA mass ratio (90/10) employed for this test was chosen to provide a sample that was relatively sensitive to shock initiation. Previous studies indicate that the 90/10 ratio is close to optimal in providing a sensitive formulation.[16]

After sample formulation, the sample was drawn into a 5-mL glass syringe with a fluorocarbon plunger and immediately transferred to the light gas gun laboratory. Using a small vacuum pump, the target assembly was evacuated through one of the two 1/16” OD fill tubes that had been installed into the sample cell. Luer-Lock and Swagelok® fittings were used to connect the syringe. Chemically-resistant PVDF (poly(vinylidene fluoride)) Luer-Lock stopcocks on each of the fill tubes allowed the vacuum side to be closed to the pump and for the fill side to then be opened. The fill side of the assembly was carefully opened with the vacuum side open. As soon as material was observed to move through the syringe, the vacuum side stopcock was closed. This operation was performed to minimize introduction of the small amount swept-volume air that was impossible to evacuate from the fill-side stopcock. With the force of the residual vacuum in the cell, roughly one-third of the material smoothly flowed into the target. The syringe plunger was depressed until material was observed rising into the transparent needle connector and stopcock on the vacuum side. Both stopcocks were then closed and the fill syringe and vacuum tubing removed from the assembly. Swagelok® caps were used to seal the target after filling. A photograph of a fully assembled target is shown in Fig. 11.

Single-point VISAR was used to measure the transmitted wave profile. Fiber probes were used to deliver the VISAR source illumination to the window interface and to collect the reflected light. Line-imaging ORVIS was also employed on this test using the dichroic beamsplitter arrangement shown schematically in Fig. 1.

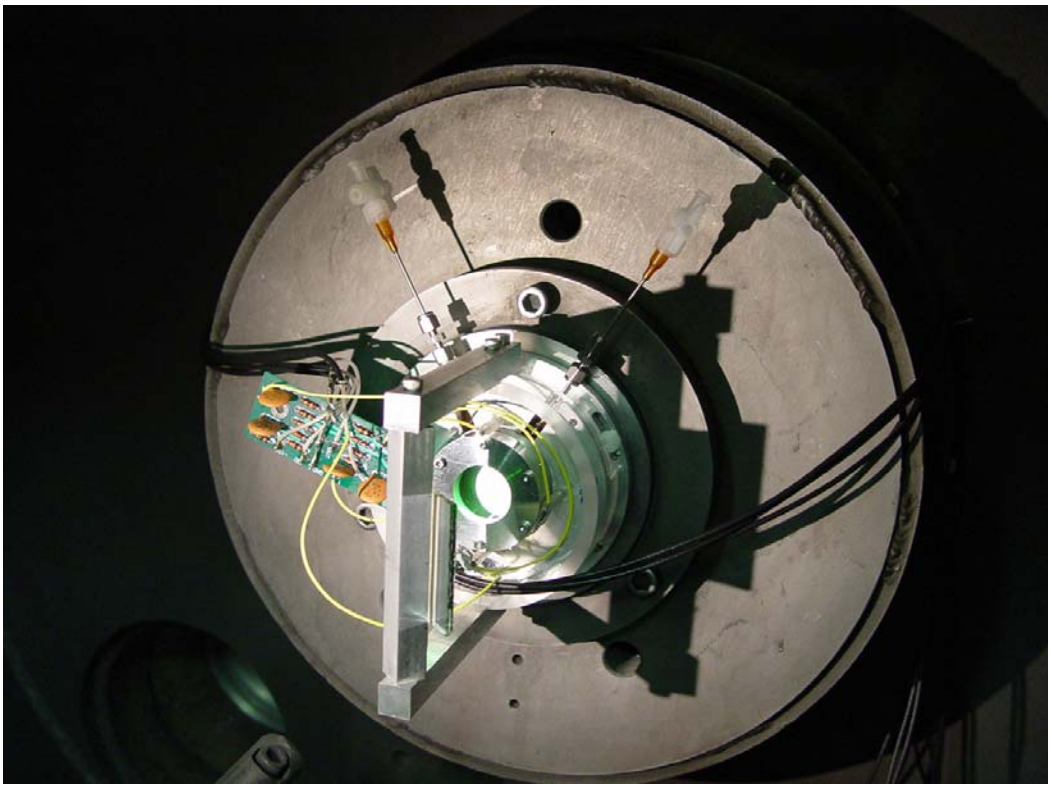

Figure 11. Assembled target mounted at the gas-gun target chamber.

The VISAR data proved to be difficult to analyze and interpret as a result of very severe light loss that occurred as the wave reached the interferometer window. From comparison of signals from the two legs of the dual-delay-leg VISAR, the most plausible transmitted wave profile is shown in Fig. 12. Unlike typical profiles obtained with tin sphere arrays (cf. Fig. 3), the particle velocity curve exhibited a fairly sharp shock with little or no precursor. Ordinarily, these characteristics (and the early peak in particle velocity) might be taken to indicate the development of a vigorous reactive wave; however, the very long time required for the wave to propagate across the 6.35-mm thickness of the sample cell and the relatively low apparent peak particle velocity are convincing evidence that this is not the case. In fact, the measured wave transit time of 5.08 μs is far slower than the 1.93 μs that would be expected from direct shock loading of pure NM (using the shock velocity from the known Hugoniot properties of NM[17] and assuming no reaction) under these impact conditions. The line-imaging ORVIS record was consistent with the VISAR data. With the current instrumentation, the ORVIS diagnostic is limited to a recording time of 4 μs. Setting the trigger delay for a possible early event, we observed no fringe displacement in the measurement window—a complementary indication of a long wave transit time. Evidently the sample geometry corresponding to a NM/DETA fill of the open volume of the tin sphere array is not favorable to initiation and sustained reaction of the explosive mixture.

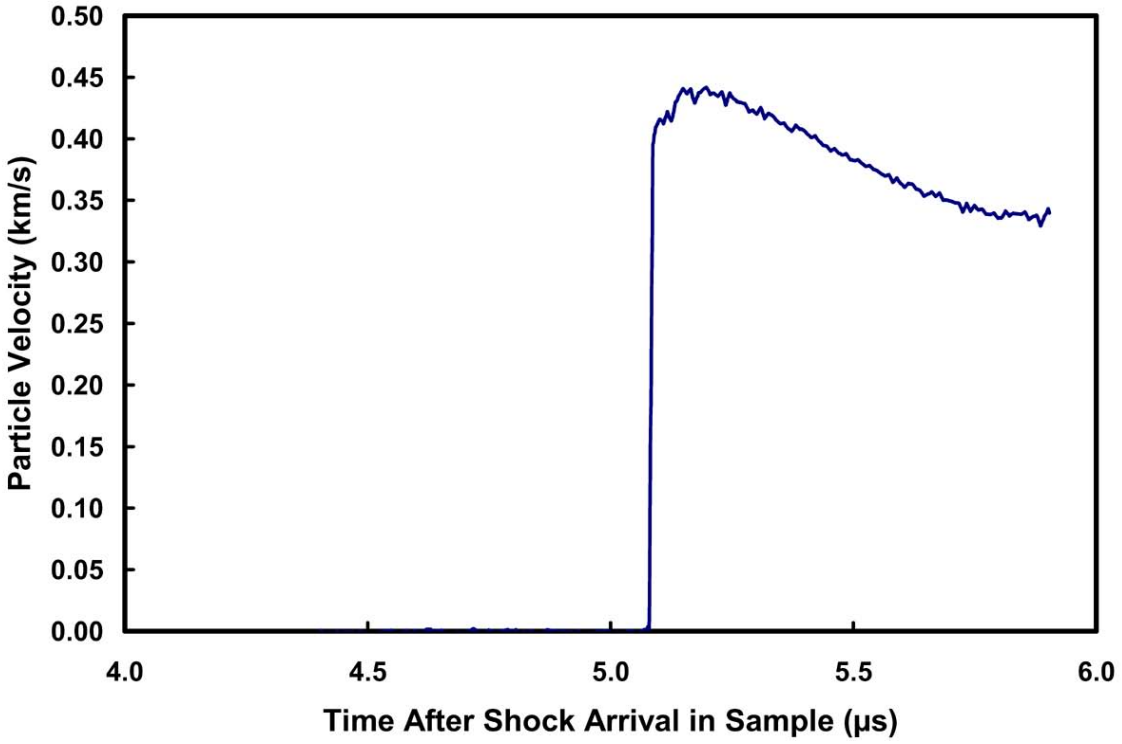

Figure 12. Particle velocity of wave transmitted by 6.35-mm-thick tin sphere bed with NM/DETA (90%/10%) fill displacing packed bed porosity (as measured by single-point VISAR).

The negative result of our preliminary test with NM/DETA in the tin sphere array does not rule out this deterministic geometry scheme as a possible method for studying reactive chemistry. Perhaps the regular structure of a precisely packed *fcc* or *hcp* lattice would more readily allow "hot spots" to develop, grow, and coalesce. A more shock sensitive liquid or solid explosive might yield positive results as well. Nevertheless, it is apparent that successful implementation of this scheme will require substantially more design and development together with improved availability of candidate energetic materials such as spherical nitrocellulose, etc. As a result, we have explored other options for investigating initiation and reaction growth in a deterministic geometry. Promising results of a deterministic geometry defined by sample cell inserts with periodic porosity are discussed in the following section.

4. Experiments with Robocast Inserts

A second, very promising design involved NM infiltration of a sintered aluminum oxide (Al_2O_3) fixture with a well-defined periodic porosity. This concept relies on reproducible fabrication of inserts with precisely engineered geometric properties for use in a sample cell such as that shown in Fig. 10. The Robocasting process[18] developed at Sandia National Laboratories is a unique, enabling capability for development and testing of this concept.

4.1 Robocast Insert Design and Fabrication

Sample cell inserts were fabricated out of aluminum oxide using a Sandia-developed rapid-prototyping process called Robocasting. In this process, an XYZ positioning system is used to extrude colloidal slurries through an orifice to form 3-dimensional parts in a layer-wise manner. The parts are dried and sintered, usually in ~12 hours. A schematic of a Robocasting machine capable of dispensing up to four materials simultaneously can be seen in Fig. 13. This technology has progressed from its original design to include several different types of deposition heads, allowing for spraying, microjet application, precision writing, and the original slurry extrusion of materials, all from the same platform. Incorporation of post build machining and an additional fourth and fifth axis are current capability developments.

For the NM infiltration studies, it was necessary to create structures with a well-controlled periodic porosity. The rheological characteristics of the slurry were adjusted so that as the material was extruded from the nozzle; it could span gaps in the layers below as shown in Fig. 14. The alumina slurry was patterned into disks that, after sintering, were nominally 6.0 mm in height and 24.9 mm in diameter to provide a close fit to the sample cell of 6.35 mm height and 25.4 mm diameter. Each disk was comprised of a lattice of rods bounded by a ring. The ring had two notches that were cut after the disk was Robocast and sintered to create an infiltration path into the lattice area. The lattice rods in the interior of the ring were 0.75 mm in diameter and had a gap of 0.75 mm between rods of the same layer. Spacing between every other layer was designed to be 0.5 mm as shown in Fig. 15. Sintering of the alumina slurry was performed at 1650ºC with a two hour hold to yield material > 98% dense. The overall geometric density was designed to be 54%. A computer-aided-design (CAD) diagram and a photograph of a completed insert are shown in Fig. 16.

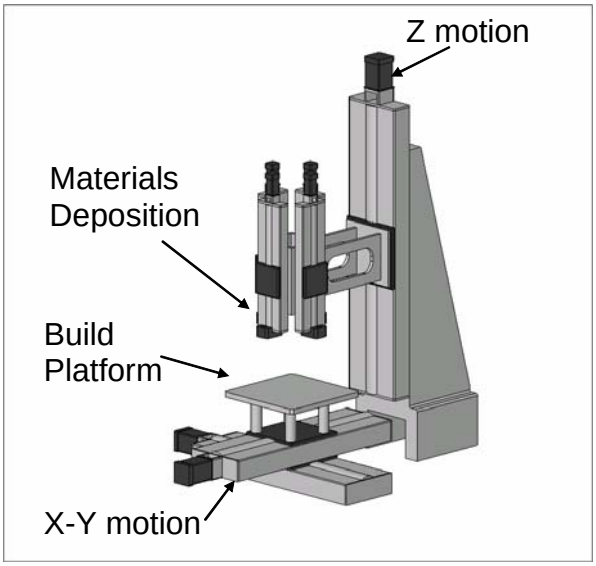

Figure 13. Schematic of a Robocaster capable of dispensing four materials or accepting deposition heads allowing for other means of printing materials.

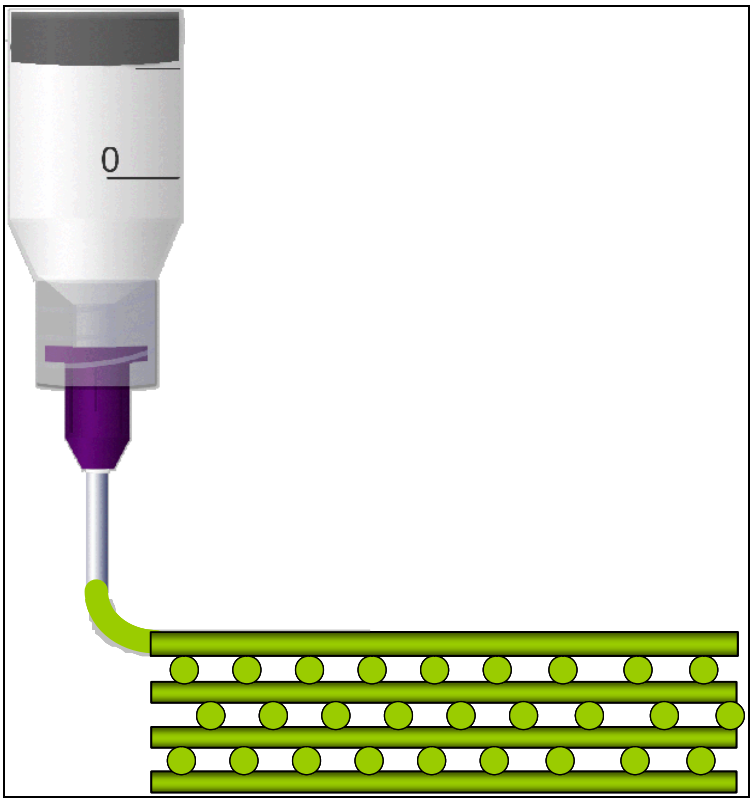

Figure 14. Schematic representation of a self-supporting slurry spanning gaps to form a structure with periodic porosity using the Robocasting process.

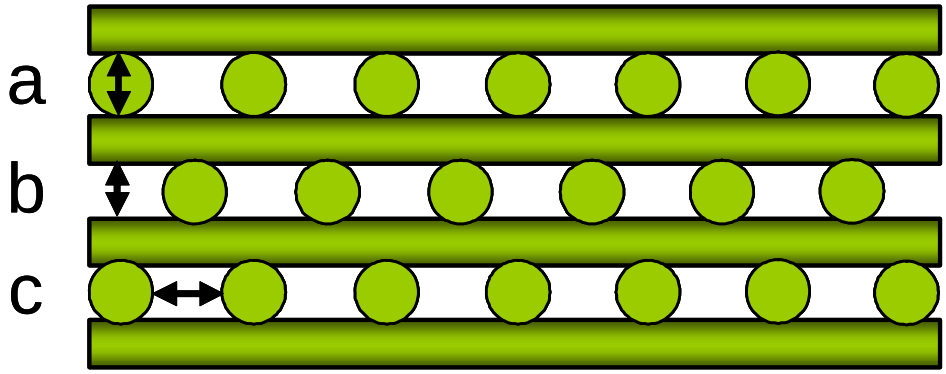

Figure 15. Dimensions of the Robocast lattice utilized in this study are (a) 0.750 mm, (b) 0.50 mm, (c) 0.75 mm.

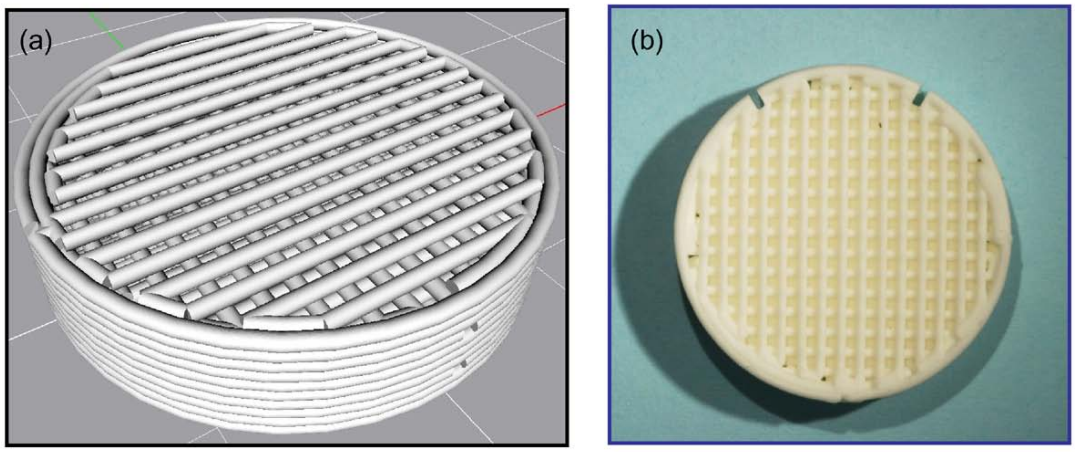

Figure 16. (a) CAD representation of Robocast insert for gas-gun target assembly; (b) photograph of completed part.

4.2 Target Assembly and Preliminary Fill Test

Each Robocast Al_2O_3 insert was installed in an aluminum sample cell such as that illustrated in Fig. 10. The NM-compatible Barco Bond 5-minute epoxy was used to bond the perimeter of the insert to the sidewall of the cell. The sintering process used in the insert fabrication produced a slight concavity on one side of the device. We positioned each insert so that the more planar side was in contact with the cell floor. Since the inserts were designed to be slightly undersized in thickness (compared to the 6.35-mm-thick cell), this orientation resulted in a fairly significant open volume (defined by the cell diameter and a length of ~0.5-0.7mm) adjacent to the Kapton/PMMA interferometer window. We also oriented the inserts to align the grid defined by the topmost lattice rods perpendicular to the direction corresponding to the line segment used in the line-imaging ORVIS setup. This step served to align the two notches of the insert (cf. photograph in Fig. 16) to the sample-cell fill holes as well. A total of six target assemblies with Robocast inserts were prepared for gas-gun impact tests.

Similar to the procedure described in Section 3, the plan for sample loading called for an initial evacuation of air pressure from the cell followed by liquid infiltration. Before final assembly of one of our fixtures, we installed a clear PMMA window and performed a preliminary fill test with water. A photographic sequence of the liquid infiltration is shown in Fig. 17. This procedure verified that the filling technique effectively sweeps away air in the cell, leaving the filled volume essentially bubble free.

4.3 Sample Formulation and Loading

The availability of six essentially identical target fixtures facilitated a direct comparison of sensitized NM and the “baseline” case of NM alone. For the NM samples, NM (Aldrich, 99+%) was used without further purification. For the NM/DETA samples roughly 3 mL of NM (Aldrich, 99+%) and 5% (by mass) DETA (Aldrich, 99%) were combined in a 20 mL vial. The vial was stirred with a Teflon-

coated stir bar on a magnetic stirring plate for five minutes. This sample preparation was always performed immediately before target loading and a fresh sample was prepared for each experiment. Table 1 provides a formulation summary for the gas gun experiments.

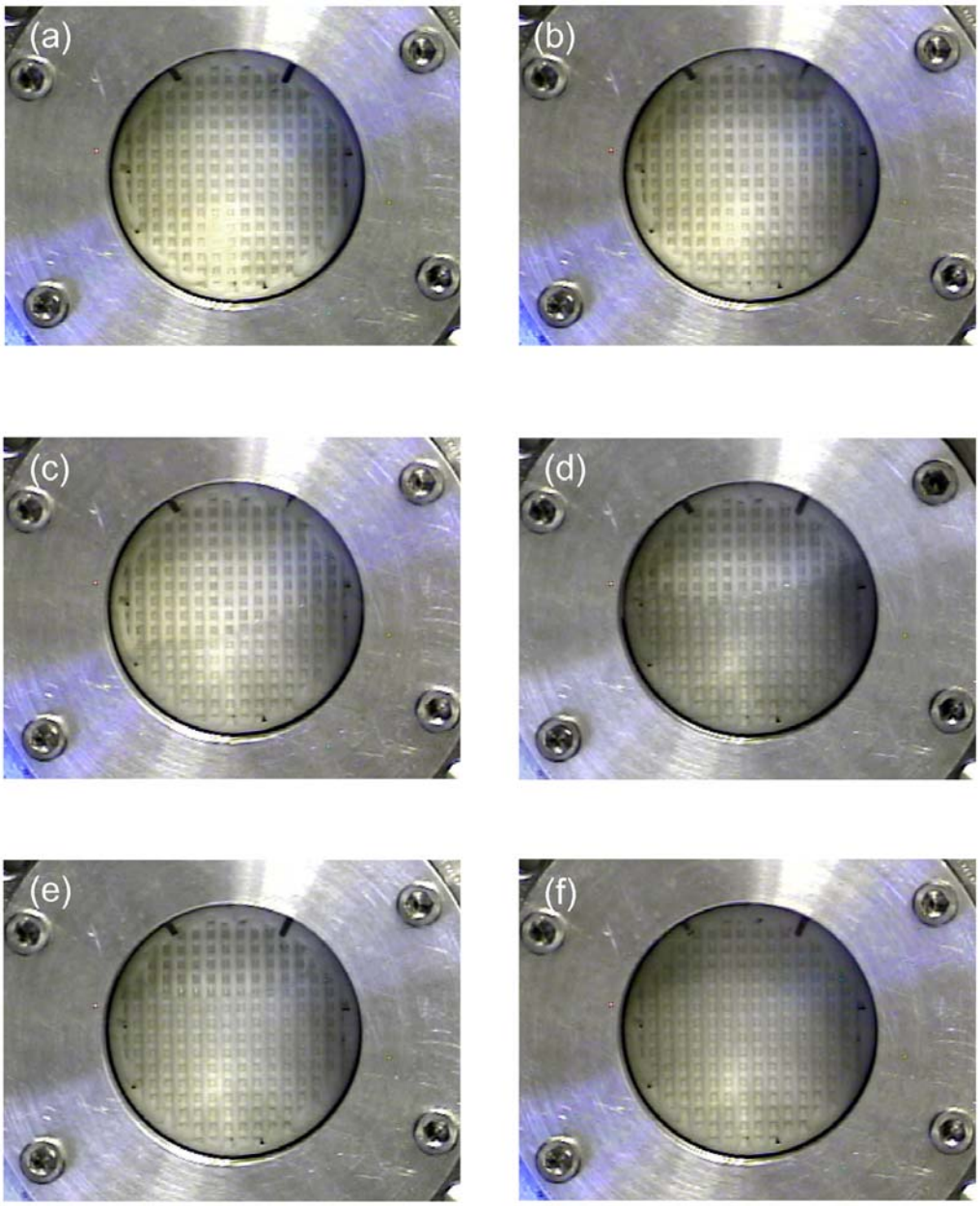

Figure 17. Photographic sequence demonstrating uniformity of liquid fill in gas-gun target assembly: (a) view of Robocast insert in sample cell prior to filling; (b) liquid present at top fill slot and along bottom of cell; (c) cell nearly half filled; (d) cell approximately two-thirds filled; (e) liquid fill approaching completion; (f) filled cell exhibiting good uniformity.

Table 1. Formulation Summary for Light Gas Gun Experiments

Date	Shot Number	Sample (ratios reflect mass percent)	Projectile Velocity (km/s)	NM (g) -------- (% wrt DETA)	DETA (g) -------- (% wrt NM)	Wave Profile Diagnostic
4/28/2005	440	NM/DETA (90/10) in Tin Ball Bed (hybrid close packed)	1.207	2.527 -------- 90.09	0.278 -------- 9.91	VISAR & ORVIS
8/9/2005	452	NM with Robocast Alumina Insert	1.186	2.800 -------- 100.00	-------- 0.00	VISAR
8/10/2005	453	NM/DETA (95/5) with Robocast Alumina Insert	1.182	3.144 -------- 94.87	0.170 -------- 5.13	VISAR
8/15/2005	454	NM with Robocast Alumina Insert	1.189	2.500 -------- 100.00	-------- 0.00	VISAR & ORVIS
8/16/2005	455	NM/DETA (95/5) with Robocast Alumina Insert	1.004	3.172 -------- 94.97	0.168 -------- 5.03	VISAR & ORVIS
8/24/2005	456	NM/DETA (95/5) with Robocast Alumina Insert	0.793	3.373 -------- 94.99	0.178 -------- 5.01	VISAR & ORVIS
8/25/2005	457	NM with Robocast Alumina Insert	0.792	2.800 -------- 100.00	-------- 0.00	VISAR & ORVIS

NM = nitromethane, Aldrich 99+%
DETA = diethylenetriamine, Aldrich 99%

Sample loading for the series of experiments with Robocast inserts was performed in a manner very similar to that used for the gas gun test discussed in Section 3. Once again, the formulated sample was drawn into a 5-mL glass syringe with a fluorocarbon plunger and immediately transferred to the light gas gun laboratory. The sample cell (already mounted at the end of the gas gun barrel) was evacuated and then filled with NM or NM/DETA using the hardware and procedure already described. The sample-cell hardware maintained leak-tight conditions on all tests; the large gas-gun target chamber is evacuated prior to firing and it achieved a vacuum better than 50 mTorr in each case.

4.4 Transmitted Wave Profiles: Results and Discussion

Shock loading tests were performed (using an aluminum projectile/impactor in all cases) at impact velocities ranging from 0.79-1.19 km/s. Three samples contained NM alone and three were tested with NM/DETA, as shown in Table 1. Single-point VISAR was employed on all six tests while line-imaging ORVIS was used on the last four. Tests in which both diagnostics were fielded made use of the dichroic beamsplitter device shown schematically in Fig. 1.

The observed wave profiles are very complex and reveal globally dispersive but strongly organized (locally) stress states generated by shock propagation through the well-defined, millimeter-scale matrix. Similar to the previously-described test with NM filling the voids in the tin sphere array, the VISAR signals were generally difficult to analyze. Figure 18 shows a representative set of signals from one of the legs of the

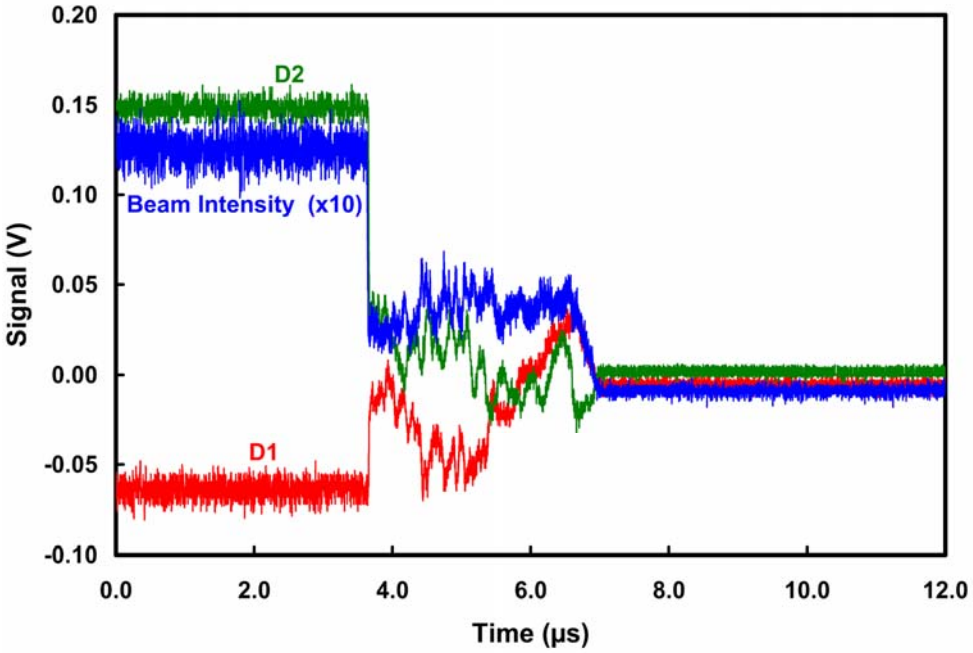

Figure 18. Signals from quadrature-coded VISAR channels and beam intensity monitor for NM/DETA/Robocast test; Impact Velocity = 1.004 km/s.

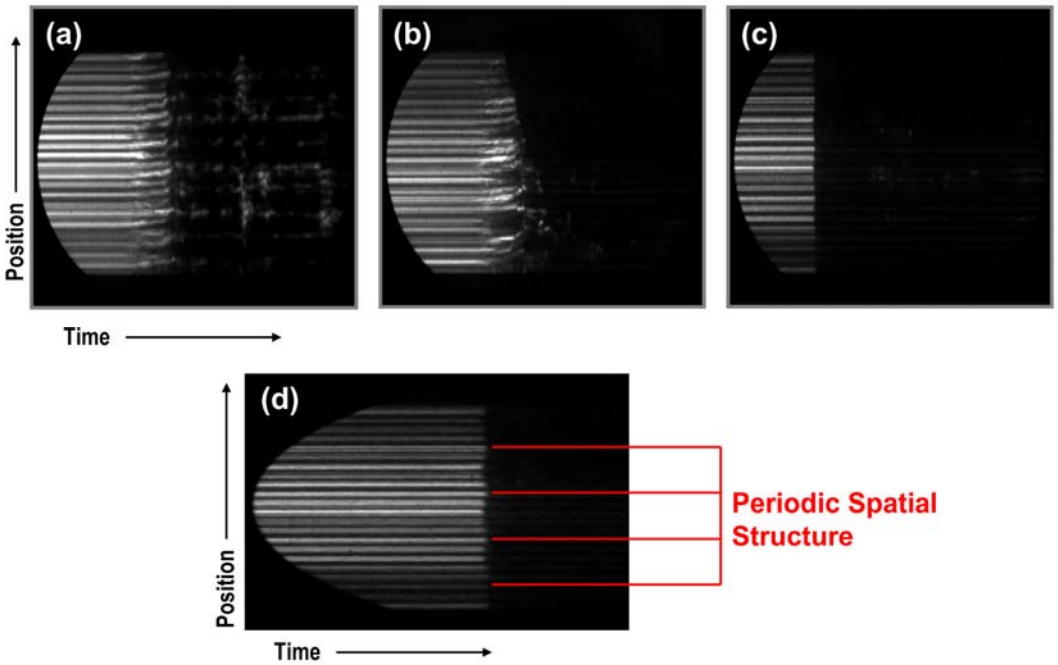

Figure 19. Line-imaging ORVIS fringe records from a series of tests with Robocast inserts: (a) NM fill—Impact Velocity = 0.792 km/s; (b) NM/DETA fill—Impact Velocity = 0.793 km/s; (c) NM/DETA fill—Impact Velocity = 1.004 km/s; (d) Vertically compressed view of fringe record from NM/DETA fill—Impact Velocity = 1.004 km/s.

dual-delay system. D1 and D2 correspond to the quadrature-coded fringe intensity signals of the system (with D2 retarded by 90^o in phase). The beam intensity signal represents a small portion of reflected light that is not sampled by the interferometer. This trace is useful in discriminating actual fringe motion vs. a simple time-dependent loss in target reflectivity. The signals in Fig. 18 illustrate the severe loss in reflected light upon arrival of the main shock (occurring at ~3.7 μs on the plotted time base) that we typically observed in this series of tests. Useful recording times of 3 – 4 μs were obtained before complete loss of reflected light occurred. High-frequency "noise" and apparent small-level DC bias on the signals were additional complications. Considerable effort was devoted to processing the raw signals for optimal data reduction. Steps included (1) averaging the late-time signals to arrive at a useful estimate of the DC bias for each channel followed by subtraction of this value in each case and (2) removing the high-frequency noise from the signals through a Wavelet 1-D Packet analysis (Wavelet Toolbox, MATLAB® product family, The Math Works, Inc., Revision 13) using the Daubechies3 wavelet transform. The latter processing step was extremely effective in suppressing the high-frequency component without over-smoothing the lower frequency oscillations that evidently arise from velocity fluctuations. The reduced VISAR velocity-time profiles are discussed below.

The line-imaging ORVIS fringe records provide a complementary view of the complex transmitted waves. Some representative records that illustrate differences observed for NM vs. NM/DETA as well as the effect of increased impact velocity are shown in Fig. 19. Fringe motion corresponds to induced material velocity at the sample/window interface (modulated slightly by the Kapton buffer). At the lower impact velocities, slow-rising "precursors" to the main shock wave are present. This motion is clearly not uniform along the line segment of the laser probe (i.e., along the vertical orientation in the image data). Regions of more vigorous and dispersive growth in particle velocity are evident in the NM/DETA record shown in Fig. 19b. The severe light loss upon arrival of the main shock is clearly seen as well. The dynamic range of the streak camera/intensifer/CCD camera recording system used in line-imaging ORVIS is significantly less than that available to the VISAR system. As a result, fringe data after main shock arrival were extremely dim. Only marginal signal was available in the image shown in Fig. 19a; even poorer results were obtained in the other records. In addition to severe light loss, the post-shock fringe contrast in Fig. 19a is very low. This "fuzzy" fringe behavior strongly suggests significant velocity dispersion over the length scale associated with the fringe spacing (set to ~300 μm/fringe by the target magnification used for these tests).

The basic ORVIS image data provide several other interesting observations. From the gas gun target pin data and measurements of electronic and optical signal propagation times, the time-of-arrival of the precursor motion and main shock seen in the line-imaging ORVIS records can be compared to the corresponding VISAR signals. The derived wave transit times are generally consistent to within a few tens of nanoseconds. Values for the six tests in this series are listed in Table 2. In the case of NM/DETA, a much higher wave speed is observed at impact velocity = 1.004 km/s vs. impact velocity = 0.793 km/s. At the higher impact condition, the shock wave evidently overruns the precursor-like features and becomes very sharp (cf. Figs. 19b and 19c). The ORVIS images also show that the transmitted waves exhibit relatively little large-scale curvature

across the full line segment. On the other hand, a periodic spatial structure with a characteristic length of 1.5mm is quite evident, especially in the sharp-shock case shown in Fig.19c (this image is compressed vertically for visual clarity in Fig. 19d). This length scale corresponds exactly with the characteristic transverse rod spacing of the Robocast alumina insert (cf. Fig. 15).

Table 2. Wave Profile Characteristics for Shock Loaded NM and NM/DETA Samples

Shot Number	**Sample** (ratios reflect Mass percent)	**Projectile Velocity** (km/s)	**Predicted Particle Velocity in PMMA**[a] (km/s)	**Measured Particle Velocity in PMMA**[b] (km/s)	**Predicted Wave Transit Time**[a] (μs)	**Measured Wave Transit Time**[c] (μs)
440	NM/DETA (90/10) in Tin Ball Bed (hybrid close packed)	1.207	0.877	0.44	1.931	5.08
452	NM with Robocast Alumina Insert	1.186	0.862	?[d]	1.971	1.77
453	NM/DETA (95/5) with Robocast Alumina Insert	1.182	0.860	?[d]	1.948	1.39
454	NM with Robocast Alumina Insert	1.189	0.864	1.05	1.969	1.81
455	NM/DETA (95/5) with Robocast Alumina Insert	1.004	0.731	1.48	2.090	1.43
456	NM/DETA (95/5) with Robocast Alumina Insert	0.793	0.577	0.75	2.292	2.02
457	NM with Robocast Alumina Insert	0.792	0.575	0.75	2.329	2.03

a. Assuming no reaction in the NM or NM/DETA sample and no inert filler or insert
b. Corresponds to measured velocity attained immediately after sharp rise in particle velocity
c. From time of shock arrival in sample to time corresponding to sharp rise in particle velocity (i.e., neglecting precursor)
d. Actual particle velocity uncertain—inconsistent results from the two VISAR legs

Given the poor fringe intensity and contrast after the arrival of the main shock, we restricted analysis of the spatially resolved particle velocity in the ORVIS data to the precursor region. A spatially resolved velocity profile for the NM/Robocast test at impact velocity = 0.792 km/s is shown in Fig. 20. In this case, the onset of low-velocity material motion precedes the main shock by approximately 500 ns. Complex wave structure across the line segment is evident as well. Projection of the color-coded velocity onto the time-position (xy) plane provides a revealing view of this structure, as shown in Fig. 21. The basic fringe record (Fig. 21a) is scaled along the position axis to match the velocity plot in this graphic representation of the data. The 1.5-mm-scale structure evident in the intensity fluctuations displayed in Fig. 19 is also apparent in the velocity profile. Smaller scale spatial structures along the line segment also appear to be present in the precursor region. Similar organized behavior was observed with the NM/DETA sample at impact velocity = 0.793 km/s; however, the wave growth seemed to be somewhat more chaotic overall and more vigorous at certain locations along the line segment (cf. Fig. 19b). The observed velocity fluctuations indicate that shock propagation through the NM-filled or

NM/DETA-filled Robocast rod array imprints a distinctive pattern on the wave structure through shock interactions in the periodic matrix.

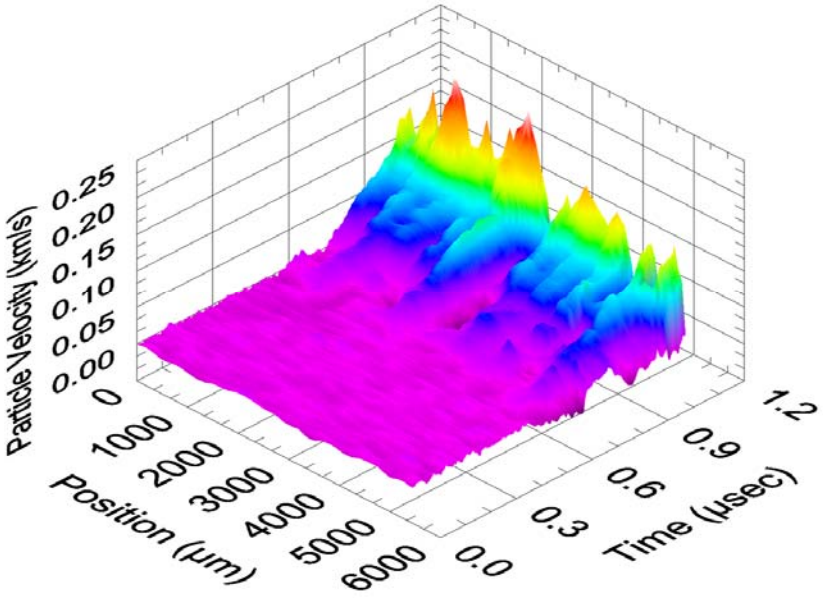

Figure 20. Spatially resolved velocity profile showing precursor region of wave transmitted by NM/Robocast sample; Impact Velocity = 0.792 km/s. The origin of the time axis is not correlated with shock arrival in the sample on this plot.

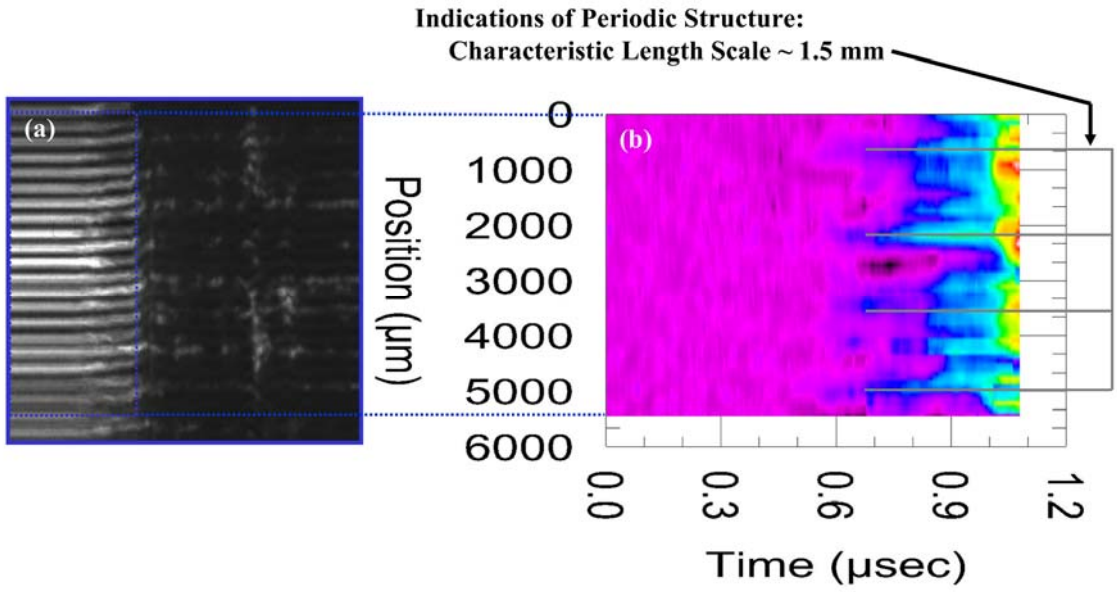

Figure 21. (a) Line-imaging ORVIS fringe record of wave transmitted by NM/Robocast sample—Impact Velocity = 0.792 km/s; (b) Corresponding spatially resolved velocity profile—color coded and projected onto time-position plane.

The higher dynamic range of the VISAR diagnostic proved valuable in measuring the particle velocity after arrival of the main shock at the interferometer window. VISAR velocity-time profiles for NM/Robocast samples at two different impact conditions are plotted in Fig. 22. Consistent with the line-imaging ORVIS record, the VISAR signal at the lower impact condition exhibits a lengthy (~500 ns duration), slow-rising precursor to the main shock wave. The main shock itself is not instantaneous, indicating some dispersion in the stress states. Significant fluctuations are apparent on the particle velocity plateau; these fluctuations are typically separated by a few hundred nanoseconds. Since shock velocities in NM are ~3 mm/μs at these impact conditions, the period of the observed fluctuations would correspond to a length scale of 0.5-0.75mm in this material. This correspondence once again strongly suggests the presence of shock interactions associated with the length scales of the Robocast alumina lattice. Apart from these fluctuations, the particle velocity is relatively constant after the main shock arrival; however, the velocity may be increasing slightly, reflecting the presence of some low level exothermic reaction. At higher impact conditions, the wave behavior generated by the NM/Robocast sample is markedly different. A substantially higher shock speed is evident; in fact, the wave nearly outruns the precursor. The transmitted wave exhibits higher particle velocity overall, as well as more pronounced fluctuations superimposed on the slowly increasing velocity after shock arrival. These features are consistent with an increased level of energy release.

Figure 23 compares two VISAR records obtained from NM/DETA samples containing the Robocast insert at two different input conditions. The results obtained at the lower impact condition (impact velocity = 0.793 km/s) can be directly compared with the NM trace (Fig. 22) at essentially the same shock level. The peak particle velocity is very nearly the same in both cases; however, as already discussed in connection with the ORVIS image data (cf. Figs. 19a and 19b), the precursor to the main shock exhibits both higher particle velocity (locally) and a more complex wave growth in the NM/DETA formulation. At impact velocity = 1.004 km/s, NM/DETA generates a wave with much higher shock speed (completely overrunning any precursor behavior, cf. Fig. 19c) and much higher particle velocity. The transmitted wave also shows steady growth behind the shock front as well as persistent temporal fluctuations. The higher speed, higher particle velocity and steady growth provide compelling evidence that initiation and sustained exothermic reaction have occurred in this case. The transmitted reaction-driven wave is clearly more vigorous than that generated by NM alone at a significantly higher impact velocity (1.189 km/s, cf. Fig. 22). This behavior is consistent with the known increased shock sensitivity of NM/DETA vs. NM; for example, addition of 5% DETA causes the shock pressure required to generate detonation in 1 μs to decrease from ~10 GPa to ~7 GPa.[19] In this regard, it is interesting that the peak particle velocities generated by NM and NM/DETA at the lower shock inputs in our tests are very similar. This may indicate that only nascent and intermittent conditions of initiation and reaction growth are being triggered under these conditions.

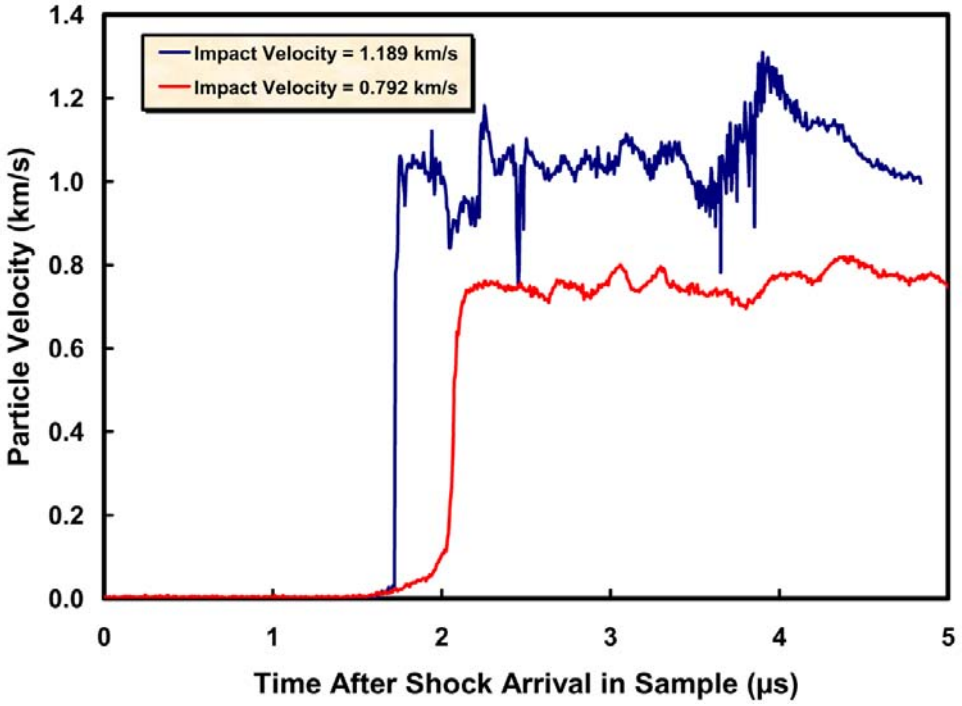

Figure 22. Comparison of VISAR velocity-time records obtained from NM/Robocast samples at two different impact conditions.

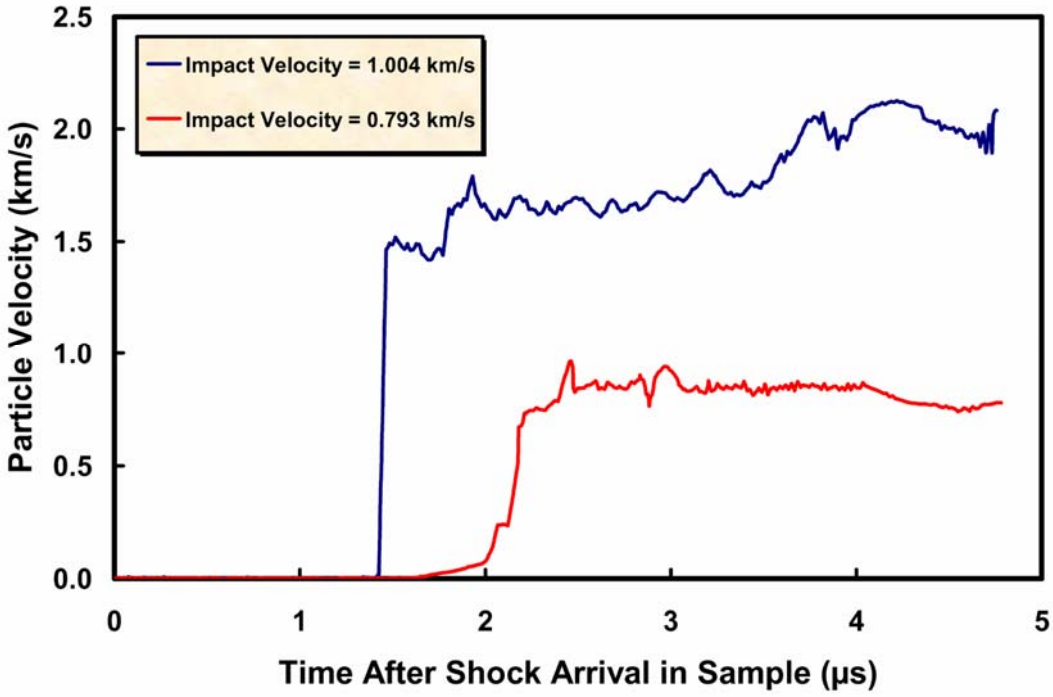

Figure 23. Comparison of VISAR velocity-time records obtained from NM/DETA/Robocast samples at two different impact conditions.

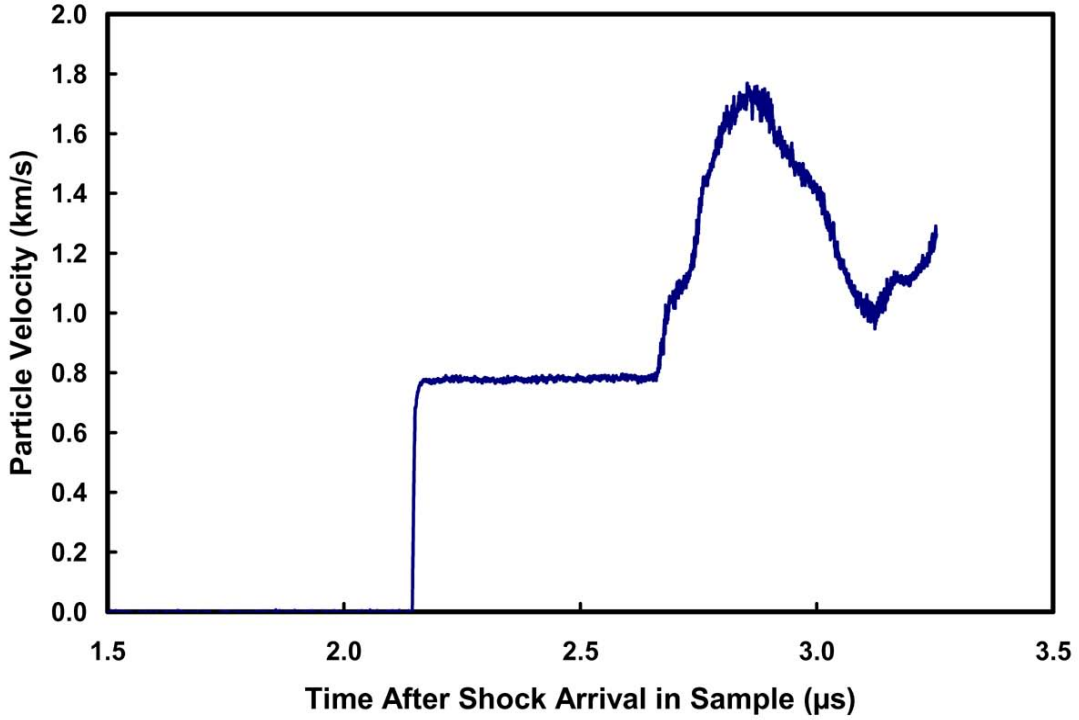

Figure 24. Transmitted wave profile from 6.35-mm-thick sample of gelled nitromethane under impact at 1.112 km/s (as measured by single-point VISAR).

To place the complex wave profiles observed in this work in better context, it is instructive to review briefly results of previous NM shock-loading studies[15] performed using the identical sample cell design and similar impact conditions but *without* the Robocast insert. The wave profile plotted in Fig. 24 is characteristic of NM material response under these conditions. The test sample in this case was actually NM gelled with 3% finely dispersed PMMA; however, pure NM and NM/DETA are known to respond in a very similar manner.[19] With the gelled NM, we observed a sharp shock followed by a plateau of constant particle velocity corresponding to a state of shock compression without reaction. The subsequent, rapid increase in particle velocity (cf. Fig. 24) was generated as a result of reaction initiation occurring at shock-focusing sites in the corners of the aluminum sample cell near the impact interface (cf. Fig. 10) followed by vigorous energy release. This type of wave behavior is consistent with the classic description of homogeneous explosive initiation[20] wherein the explosive material is shocked and, after an induction period, a thermal explosion occurs at or near the explosive/driver interface. After the explosion, the high-velocity reactive wave runs forward into the precompressed explosive. With sufficient run distance, the high-velocity wave overtakes the initial shock and then decays to a steady detonation wave. With targets including the Robocast insert, the NM and NM/DETA wave profiles do not fit this simple picture. Indeed, the transmitted wave from NM/DETA at impact velocity = 1.004 km/s strongly resembles the typical profile of *heterogeneous* explosive initiation wherein energy release first occurs at "hot spots" distributed in the compressed material.

Subsequent growth and coalescence of these reactive regions result in less abrupt wave growth behind the front. In this initiation and growth regime, energy release gradually accelerates and steepens the initial wave front.

Additional insight can be gained from considering equation-of-state properties of NM in conjunction with a stress-particle velocity Hugoniot diagram that illustrates (in an idealized form) the shock processes occurring at the sample/window interface in our target fixture (neglecting the effect of the alumina insert). A plot that reflects the expected shock interactions at impact velocity = 1.2 km/s is shown in Fig. 25. Hugoniot curves for aluminum (6061-T6), NM and PMMA are taken from the compilation by Marsh, et al.[17] For NM/DETA, a corresponding curve can be generated from the estimated Hugoniot relationship described in Sheffield et al.[19] The thin layer of Kapton is approximately impedance matched to PMMA and is neglected in the diagram.

The idealized graphical analysis in Fig. 25 involves several assumptions: (1) chemical reaction in NM is neglected; (2) the Hugoniot and isentrope of aluminum are essentially identical--i.e., a shock unloads along the Hugoniot curve; (3) the reshock Hugoniot of the unreacted NM sample is assumed to be the same as the principal Hugoniot. For wave profiles exhibiting constant particle velocity in the "plateau" (such as that shown in Fig. 24), the first assumption is appropriate. The other simplifications are also justifiable given the modest shock pressures generated in these tests. Accordingly, the approximate shock conditions at the sample/window interface can be inferred from the various Hugoniot curves in the following manner. First, symmetric impact at 1.2 km/s should generate a particle velocity of 0.6 km/s and a stress of ~10 GPa in the aluminum sample cell. This corresponds to state "1" in Fig. 25. When the shock reaches the sample volume, a rarefaction is reflected back into the aluminum while a shock is transmitted to the NM, a condition represented by state "2." This analysis indicates an induced stress of ~3.5 GPa in the NM together with a particle velocity near 0.96 km/s. When this shock reaches the sample/window interface, the compressed NM material is reshocked and a shock propagates into the PMMA. This condition (labeled "3" in Fig. 25) corresponds to the state probed by the VISAR diagnostic. The expected interface particle velocity is 0.86 km/s with a calculated stress near 4 GPa. From the calculated particle velocity in NM corresponding to state "2" and the known shock velocity/particle velocity relationship for this material,[17] the time for the wave to transit the 6.35-mm-thick cell can be calculated. The calculated transit time and the calculated particle velocity in PMMA (for shock loading in the absence of the Robocast insert) provide two useful quantities for comparison to the observed wave behavior. This comparison is given for each impact condition in Table 2. Transit times and particle velocities observed in targets with the Robocast insert are consistently lower and higher, respectively, than the corresponding values from the simple 1-D analysis. Two plausible sources for the substantial differences in the experimental data are (1) as yet unquantified shock interactions with the alumina matrix and (2) effects of energy release. The latter source is almost certainly dominant in driving the NM/DETA wave profile at impact velocity = 1.004 km/s.

Coupled with the possible effects of explosive energy release, the complexities of material interactions involving NM (or NM/DETA) in a ~mm-scale matrix can only be addressed with 3-D numerical simulations incorporating realistic dynamic material properties and a suitable model for explosive initiation and energy release. Initial simulations of shock loading of a NM-filled alumina rod array were conducted using

numerical tools and methods[11-13] similar to those described in Section 2.3. Once again, the projectile, sample cell, and buffer/window materials were included in the problem setup. The constructed RVE included an alumina matrix comprised of ten layers of rods with each layer consisting of four rods positioned to match the geometric orientation shown in Fig. 15 and the known dimensions of the finished Robocast insert. The thin region adjacent to the buffer/window and containing only NM was included in the calculation. Periodic boundary conditions were imposed on the transverse boundaries of the RVE. Figure 26a shows the material geometry prior to impact on the lower surface.

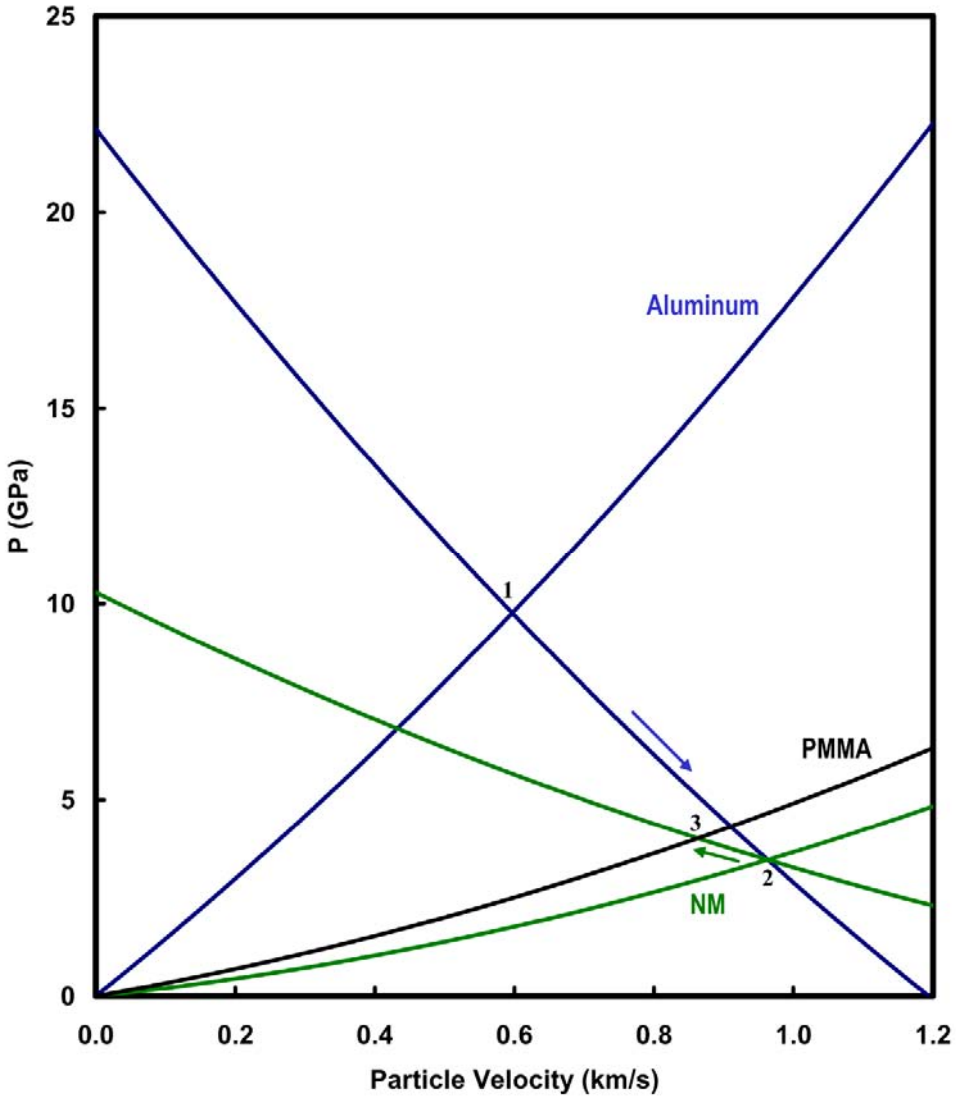

Figure 25. Idealized Hugoniot plot for understanding the expected shock interactions in the gas gun test series (at impact velocity = 1.2 km/s).

As for the modeling discussed in Section 2.3, this numerical simulation involves the implicit assumption of constitutive relationships that may be only approximate at the mesoscale. The aluminum impactor and sample cell were modeled using a Mie-Grüneisen EOS. CTH EOS database parameters (Sesame table) were used to describe the alumina, Kapton, and PMMA. The EOS description used for the alumina corresponds to fully dense, crystalline alumina. In the absence of available Hugoniot data for the actual sintered Al_2O_3, this necessary approximation may have introduced some (as yet unquantified) systematic error into the calculation. For modeling the polymers in the problem, the EOS parameters utilized the Maxwell viscoelastic description with the CTH database parameters. The NM material description included a history variable reactive burn (HVRB) model as a first approximation to the energy release properties of this explosive substance. Tracers at the Kapton/PMMA interface monitor the particle velocity and pressure conditions at the location of the VISAR and line-imaging ORVIS diagnostics.

In addition to the material geometry, Fig. 26 displays stress maps and the associated material deformation at three different times after shock arrival in the sample cell in the case of impact at 0.792 km/s (matching the impact conditions for the experimental data shown in Fig. 19a, Fig. 20, Fig. 21, and Fig. 22—lower trace). Figure 26b illustrates the complex interaction of the alumina rods with the surrounding NM. The key phenomenology includes stress bridging in the alumina rods and the formation of pockets of elevated pressure in the NM at sites of shock focusing. The precise geometric pattern of the computational lattice favors the formation of multiple “hot spots” with identical properties, a condition that is closely approximated but obviously not exactly matched in the experiment. As shown in Fig. 26c, the highly dispersive fields begin to smooth out somewhat as the wave front exits the lattice and traverses the pure NM. Even so, the effects of the regular lattice structure remain evident as the wave front reaches the interferometer window. The local, periodic structure (with its characteristic ~1.5-mm spacing; cf. Fig. 26d and Fig. 15) in the wave profile matches that seen in the line-imaging ORVIS records (cf. Fig. 19).

Plots that overlay calculated particle velocities and pressures at different tracer locations are shown in Fig. 27. A high degree of coherence is seen in the fluctuations superimposed on the main profiles. The relative amplitude of the particle velocity fluctuations is roughly comparable to those seen in the comparable VISAR record (cf. Fig.22—lower trace). The 2-μs shock arrival time also matches that seen in the experimental data. Moreover, the initial shock is not abrupt, corresponding to the dispersive behavior observed in the VISAR profile. The subtle, steady rise in both particle velocity and pressure after arrival of the main shock indicate a low level of NM energy release under these impact conditions. There are, however, two notable discrepancies in the experimental vs. simulated wave profiles: (1) the experimental precursor region is substantially more extended than that seen in the calculations and (2) the average plateau particle velocity is much higher in the experimental data. In fact, the calculated particle velocity is reasonably close to the value predicted on the basis of Hugoniot relationships of NM and sample cell materials in the absence of an alumina matrix (cf. Table 2). Two present uncertainties represent important roadblocks to resolving these discrepancies. First, an accurate EOS description of the Robocast alumina is needed. Errors in this description may be critical in propagating inaccuracies in

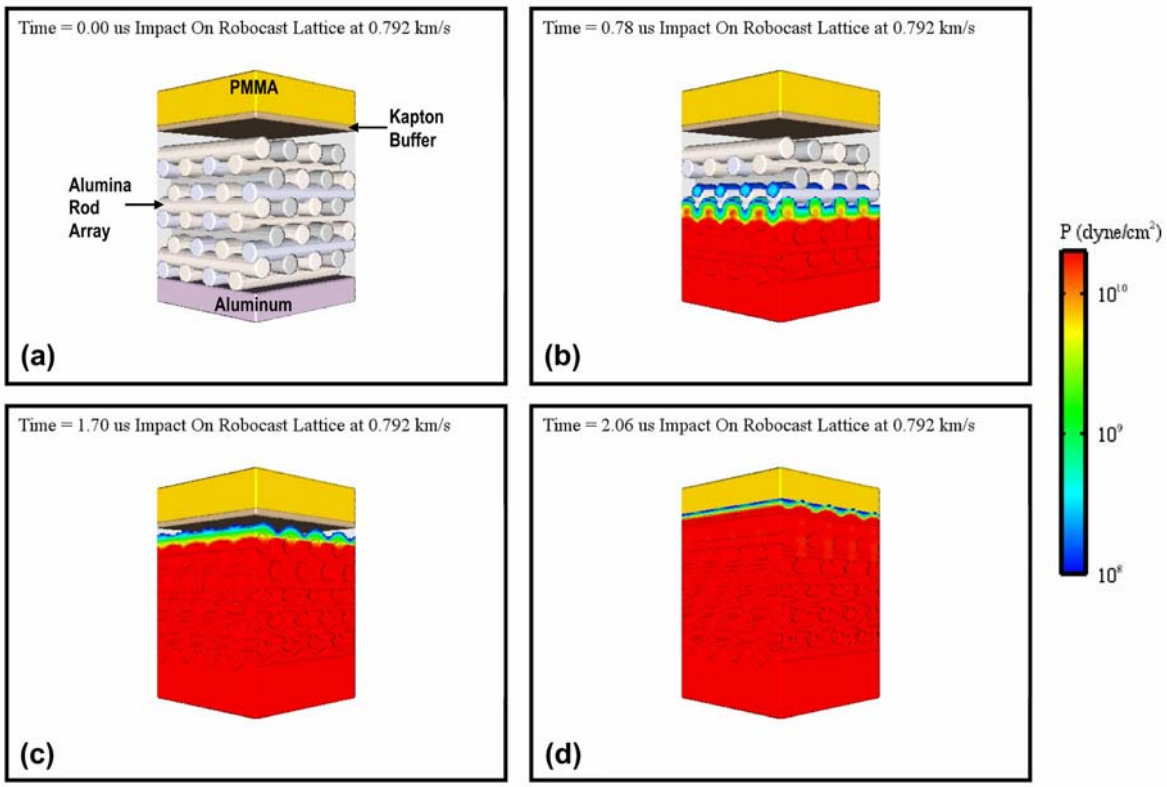

Figure 26. Numerical simulation of shock loading test with NM and Robocast alumina insert in aluminum sample cell—impact velocity = 0.792 km/s: (a) material configuration prior to impact; (b) deformation and stress contours at 0.78 μs after shock enters sample cell; (c) deformation and stress contours at 1.70 μs after shock enters cell; (d) deformation and stress contours at 2.06 μs after shock enters cell—transmitted wave is beginning to interact with the interferometer window at this time.

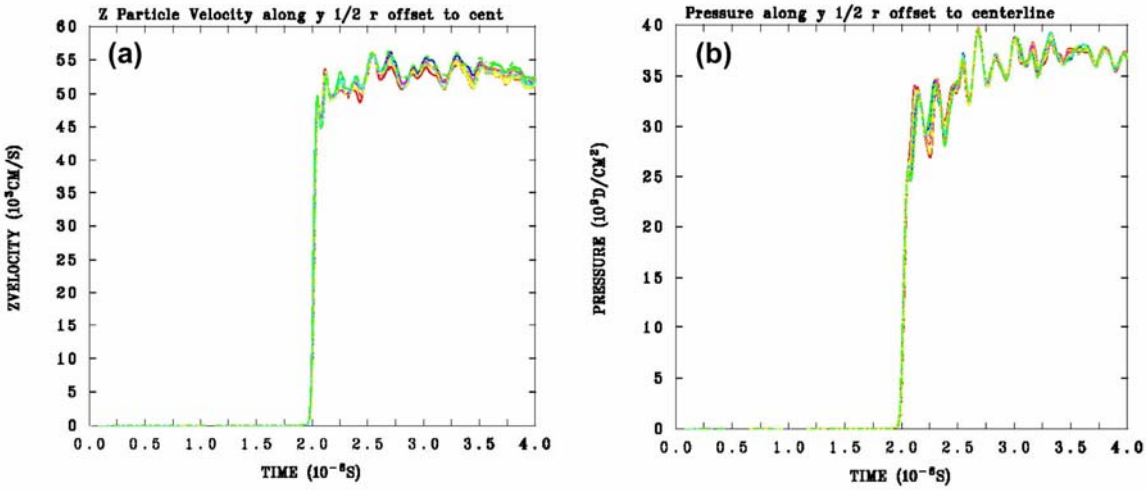

Figure 27. Calculated particle velocity and pressure histories for shock loading test with NM and Robocast alumina insert in aluminum sample cell—impact velocity = 0.792 km/s: (a) particle velocity at various locations at buffer/window interface; (b) pressure at various locations at buffer/window interface.

simulations of the magnitude and degree of dispersion of the particle velocity profile. Second, the HVRB model is very likely insufficient to capture the necessary details of nascent and intermittent energy release in this problem. This model is tailored to descriptions of detonation transfer and associates energy release too closely with the shock front. A realistic multiphase reaction model is required to describe accurately hot spot formation, growth and coalescence under the threshold-like conditions of the present study.

5. Summary

We have evaluated different approaches to preparing and testing explosive samples in a highly deterministic geometric configuration. This experimental concept is directed toward the goal of preserving the essential phenomenology of heterogeneous explosive initiation while largely constraining stochastic behavior that complicates interpretation. A design for generating well-defined "hot spots" that is also accessible to diagnostics probing their growth and coalescence would represent an important new tool for validation of models of energy release in numerical simulations of explosive initiation and performance.

The first deterministic geometry considered was the concept of incorporating spheres of explosive material in the hole locations in a close-packed bed of inert spheres. Numerical simulations indicate that a sample geometry of this type could be used to generate organized wave structures for characterization by velocity interferometric methods such as single-point VISAR and line-imaging ORVIS. Comparison of experimental data on these structures with numerical simulations could motivate the development of realistic "hot spot" models. This type of target design includes many interesting possible variations including replacement of the "host" lattice of inert spheres with energetic material spheres or filling of only one class of hole location with energetic materials. Possible designs might include highly tailored samples with deliberate inclusions or voids in the matrix. Such variations would likely aid in the interpretation of the relevant chemisty. While this design concept remains attractive, we were unable to procure spheres of energetic material in the appropriate sizes or in sufficient quantity and purity to build up the necessary gas-gun targets for experimental investigation under this one-year project. A test was performed on a surrogate design that utilized sensitized NM (90% NM/10% DETA) as a liquid explosive filler in a packed bed of tin spheres. Significant energy release apparently did not occur with this explosive material in this particular design.

A second deterministic geometry concept involved NM infiltration of a Robocast alumina matrix with a well-defined periodic porosity. Wave profiles evaluated with both VISAR and line-imaging ORVIS revealed globally dispersive but strongly organized (locally) stress states generated by shock propagation through the ~mm-scale alumina rod array. The reactive wave profiles generated under high-velocity impact strongly resemble those seen in heterogeneous explosive initiation with superimposed fluctuations indicating organized structures arising from "hot spot"-like initiation and growth on length scales corresponding to the defining alumina matrix. Generating this type of reactive chemistry with a fully dense, homogeneous explosive in a clearly defined deterministic geometry provides a unique window for investigation of fundamental

reaction mechanisms coupled to the underlying material properties and hydrodynamics. In this regard, additional work is needed to provide a satisfactory correlation of existing experimental data and the numerical simulations. This includes development of accurate Hugoniot properties for the Robocast alumina and more sophisticated reaction models that capture the important phenomenology under threshold conditions of initiation and reaction growth. Diagnostic improvements that enable acquisition of cleaner particle velocity records are needed as well.

Considerable flexibility exists in adapting the Robocast technology to this type of experimentation. The process permits facile variation of insert geometry including rod diameter, spacing, number density, etc. Precise tailoring of "hot spot" locations and sizes could provide a valuable tool in unraveling the essential mechanisms and kinetics of energy release. Possible variations also exist in materials, including both matrix and filler. Currently, the possibilities for the infiltrating explosive are fairly limited, however. NM and NM/DETA were chosen principally because these materials are liquid at room temperature and can be loaded into complex geometries at full density. Another possibility would be to use a melt-castable explosive such as trinitrotoluene (TNT), or trinitroazetidine (TNAZ); however, it would have to be melt-cast at elevated temperature and would shrink upon solidification, drawing away from the geometrically deterministic insert. To avoid the shrinkage, the experiment could be conducted at an elevated temperature with the material still liquid, but the complications associated with this assembly are beyond the scope of this project. Another possible concept involves the casting of the energetic material itself into a well-defined array with precisely controlled porosity. This deterministic geometry would likely provide useful complementary information to that obtained with the concepts explored in this project.

REFERENCES

1. Baer, M. R., "Computational Modeling of Heterogeneous Reactive Materials at the Mesoscale," in Shock Compression of Condensed Matter—1999, edited by M. D. Furnish, et al., (American Institute of Physics, Melville, NY, 2000), p. 27.
2. W. M. Trott, M. D. Knudson, L. C. Chhabildas, and J. R. Asay, in Shock Compression of Condensed Matter—1999, edited by M. D. Furnish, L. C. Chhabildas, and R. S. Hixson (American Institute of Physics, Melville, NY, 2000), p. 993.
3. M. R. Baer and W. M. Trott, in Proceedings of the 12th Symposium (International) on Detonation (Office of Naval Research Publication, ONR 333-05-2, 2005).
4. M. R. Baer and W. M. Trott, in Shock Compression of Condensed Matter—2003, edited by M. D. Furnish, Y. M. Gupta, and J. W. Forbes (AIP, Melville, NY, 2004), p. 517.
5. D. D. Bloomquist and S. A. Sheffield, J. Appl. Phys. **54**, 1717 (1983).
6. K. Baumung, J. Singer, S. V. Razorenov, and A. V. Utkin, in Shock Compression of Condensed Matter—1995, edited by S. C. Schmidt and W. C. Tao (AIP Press, Woodbury, NY, 1996), p. 1015.
7. W. M. Trott, J. N. Castaneda, J. J. O'Hare, M. D. Knudson, L. C. Chhabildas, M. R. Baer, and J. R. Asay, in Fundamental Issues and Applications of Shock-Wave and High-Strain-Rate Phenomena, edited by K. P. Staudhammer, L. E. Murr, and M. A. Meyers (Elsevier, New York, 2001), p. 647.

8. W. M. Trott, L. C. Chhabildas, M. R. Baer, and J. N. Castaneda, in Shock Compression of Condensed Matter—2001, edited by M. D. Furnish, N. N. Thanhani, and Y. Horie (AIP Press, Melville, NY, 2002), p. 845.
9. G. Diemunsch and J. P. Prenel, Optics and Laser Technology **19**, 141 (1987).
10. R. A. Lederer, S. A. Sheffield, A. C. Schwarz, and D. B. Hayes, in Proceedings of the 6th Symposium (International) on Detonation (Office of Naval Research Publication, ACR-221, 1976), p. 668.
11. J. M. McGlaun, S. L. Thompson, and M. G. Elrick, Int. J. Impact Eng. **10**, 351 (1990).
12. E. S. Hertel and G. I. Kerley, CTH EOS Package, Sandia National Laboratories Report, SAND98-0945, 1998.
13. E. S. Hertel and G. I. Kerley, Recent Improvements to CTH EOS Package, Sandia National Laboratories Report, SAND99-2340, 1999.
14. N. W. Ashcroft and N. D. Mermin, Solid State Physics (Holt, Reinhart, and Winston, New York, 1976).
15. A. S. Tappan, J. P. Wilcoxon, B. L. Abrams, S. G. Thoma, P. V. Provencio, W. M. Trott, J. N. Castañeda, S. P. Maharrey, R. Behrens, Jr., and A. M. Highley, LDRD Final Report: Nano-Scale Aluminum and Boron Clusters: Synthesis, Characterization, and Evaluation, Sandia National Laboratories Report, SAND2005-0110, 2005.
16. J. J. Lee, M. Brouillette, D. L. Frost, and J. H. S. Lee, Combustion and Flame **100**, 292 (1995).
17. LASL Shock Hugoniot Data, edited by S. P. Marsh (U. California Press, Berkeley, CA, 1980).
18. J. N. Stuecker, J. Cesarano III, and D. A. Hirschfeld, J. Mater. Process. Tech. 142, 2, 318 (2003).
19. S. A. Sheffield, R. Engelke, and R. R. Alcon, in Proceedings of the 9th Symposium (International) on Detonation (Office of the Chief of Naval Research Publication, OCNR 113291-7, 1989), p. 39.
20. A. W. Campbell, W. C. Davis, and J. R. Travis, Phys. Fluids **4**, 498 (1961).

Distribution:

1	MS 0384	A. C. Ratzel, 1500
1	0825	W. L. Hermina, 1510
1	0834	J. E. Johannes, 1512
3	0834	J. N. Castañeda, 1512
5	0834	W. M. Trott, 1512
3	0836	M. R. Baer, 1500
1	0826	S. N. Kempka, 1513
1	0834	J. S. Lash, 1514
1	0825	B. Hassan, 1515
1	0836	E. S. Hertel, 1516
1	0836	R. O. Griffith, 1517
1	1454	L. L. Bonzon, 2554
3	1454	A. S. Tappan, 2554
1	1454	R. J. Pahl, 2554
3	1349	J. N. Stuecker, 1815
1	1181	L. C. Chhabildas, 1647
1	1181	W. D. Reinhart, 1647
1	0123	D. L. Chavez (LDRD Office), 1011
2	9018	Central Technical Files, 8945-1
2	0899	Technical Library, 9616